Turbulence Characteristics of 45 Degree Inclined Dense Jets

Mingtao Jiang[1,2], Adrian Wing-Keung Law[2,3*], Adrian C. H. Lai[2]

[1]Interdisciplinary Graduate School, Nanyang Technological University, 50 Nanyang Avenue, Singapore 639798

[2]Environmental Process Modelling Centre (EPMC), Nanyang Environment and Water Research Institute (NEWRI), Nanyang Technological University, 1 Cleantechloop, Singapore 637141

[3]School of Civil and Environmental Engineering, Nanyang Technological University, 50 Nanyang Avenue, Singapore 639798

[*]Email address for correspondence: cwklaw@ntu.edu.sg Tel: +65-6790-5296

Abstract:

In the present study, we performed an extensive laboratory investigation to quantify the turbulence characteristics of 45° inclined dense jets using Particle Image Velocimetry (PIV) over a wide range of Densimetric Froude Number. The objective was to provide benchmark data to guide high resolution turbulence numerical simulations for dense jets in the future. The PIV measurements were sampled at a relatively high frequency of 50 Hz, which enabled the analysis of second order turbulence statistics as well as the turbulence kinetic energy spectrum (including the inertial subrange) along the curvilinear jet trajectory, which has hitherto not been reported. The measurements showed that the spectral profile was flat near the discharge port with the potential core, since the Kelvin-Helmholtz shear-induced turbulence at the jet boundaries had not fully penetrated to the core. The spectral profile then evolved along the trajectory with progressive steepening towards the higher frequencies, and a fully-developed profile appeared beyond the terminal rise with a clearly identifiable inertial subrange for the energy cascade. In parallel, we also performed numerical simulations using the Large Eddy Simulations (LES) approach with the Dynamic Smagorinsky sub-grid model for the specific discharge conditions as in the experiments. The LES approach followed that of Zhang et al. (2016, 2017) using GCI as the grid convergence criteria. The comparison showed that the time-averaged first order mixing characteristics of the inclined dense jet can be simulated reasonably well comparing to the experimental data. In terms of the turbulence kinetic energy spectrum, the low frequencies of the production range were also well captured by the simulations. However, the simulated transitional spectra towards the inertial subrange decayed substantially faster than the experiments. The discrepancy was attributed to the fact that the grid resolution was not sufficiently fine in the simulations (which were constrained by the available computational resources and time), such that stratified effects remained present inside the sub-grids producing additional turbulence energy that were not represented by the Dynamic Smagorinsky model. Thus, the numerical investigation showed that further improvement in sub-grid models that can incorporate the stratified effects would be desirable in the future for engineering simulations.

Keywords: Inclined dense jet, PIV, Large Eddy Simulations (LES), Turbulence Kinetic Energy (TKE), Turbulence kinetic energy spectrum.

1 Introduction

An inclined dense jet is formed by the upward discharge of dense effluents at an angle relative to the horizontal plane. The configuration has been shown to be effective in the mixing of the dense effluent with the surrounding clean ambient water so as to minimize the environmental impact, and it is now a standard practice in outfall designs e.g. for the discharge of brine effluents from desalination plants (Milione and Zeng 2008, Drami et al. 2011, Papakonstantis et al. 2011a, Christodoulou et al. 2015). Due to the engineering importance, inclined dense jets have been extensively studied in the past two decades (Roberts and Toms 1987, Roberts et al. 1997, Cipollina et al. 2005, Christodoulou and Papakonstantis 2010, Papakonstantis et al. 2011b), with the key objective to establish the optimal design of the outfall subject to the environmental regulations.

When an inclined dense jet discharges into the ambient water, it rises initially due to its upward momentum until reaching the terminal rise height. Subsequently, it falls due to the negative buoyancy, and behaves as a negatively buoyant plume. Figure 1 illustrates a schematic side view of the phenomenon. The dashed curve line is the centerline of the inclined dense jet, which is based on connecting the locus of maximum time-averaged velocity. The intersection of the jet centreline with the discharge datum is defined as the return point. The angle of inclination is θ, the jet exit velocity is U_0, and the velocity along the centerline is U_m. The horizontal and vertical coordinates of the velocity centerline are x_m and z_m, respectively.

Quantifying the second or higher order turbulence characteristics of inclined dense jets (turbulence intensity, kinetic energy spectrum, etc), is also important towards the design objective as they signify the underlying turbulence mixing. In addition, for marine species that can only withstand the contaminant concentrations for a brief period of time, the resulting turbulence environment surrounding these species also needs to be assessed. Dense jet turbulence is complex in general and encompasses eddies with a wide range of time and length scales, with influence due to the stratified effects (both stable and unstable) around the jet's boundary.

Pope (2002) described the typical profile of temporal turbulence kinetic energy spectrum. The lower frequency range of the spectrum represents the production range whereby the shear flows generate the larger size eddies that contain bulk of the turbulence kinetic energy. Towards the higher frequencies, the turbulence kinetic energy produced is then transported through the energy cascade to smaller eddies in the inertial subrange which exhibits a −5/3 slope for a high Reynolds number flow (Kolmogorov 1941, Obukhov 1941). Beyond that, a steep slope of -3 might be observed for two-dimensional eddies, before a very steep slope of -7 at the highest frequencies range which represents the viscous dissipation into heat (Heisenberg 1948).

Attempts to quantify the turbulence kinetic energy spectrum of buoyant jets had been made for vertical discharges previously. The measurement approaches included the hot-wire probes (stationary and flying) and Laser-Doppler anemometers (LDA) which are accurate point-based techniques, and Particle Image Velocimetry (PIV) which has more noise but provides an area coverage (Westerweel et al. 2013). For example, Papanicolaou (1984) used LDA to measure the axial and radial velocity fluctuations of a vertical buoyant jet. In their study, the sampling duration was more than 100 seconds, and the sampling rate was as high as 200 to 1000 Hz. With PIV, Law and Wang (2000) and Wang and Law (2002) examined the turbulence characteristics of axi-symmetric round vertical buoyant jets including the turbulence intensities in both the axial and radial directions. However, due to the limitation of laser pulsed rate, images were recorded at a relatively low sampling frequency of 5 Hz. Thus, they were not able to resolve the inertial subrange of the turbulence kinetic energy spectrum which extended to higher frequencies and thus required faster temporal measurements. Deshpande et al. (2009) reported an experimental study to investigate the mean velocity and turbulence characteristics of a jet loop reactor. Measurements were made using LDA, Hot Film Anemometry (HFA), and PIV. However, only HFA and LDA results were presented for spectral analysis. Their study showed that the appearance of the inertial subrange can be delayed close to the nozzle due to the influence of the jet core. Fellouah and Pollard (2009) studied a turbulent round air jet using the single hot wire technique with Re = 6000, 10,000 and 30,000. The turbulence kinetic energy spectrum for the axial velocity spectra was investigated at different locations between $1 < x/D < 20$. Their study showed that the energy spectrum began to display the turbulence cascade when $x/D > 3$. Similar turbulence measurements, however, had not been reported for inclined dense jets as far as we are aware.

Besides experiments, modeling studies on inclined dense jets had also been performed in recent years (e.g. Palomar et al. 2012). In particular, the use of numerical simulations with various Computational Fluid Dynamics (CFD) models to predict the mixing behavior is also becoming popular for engineering designs. Vafeiadou et al. (2005) used the software CFX with the Reynolds Averaged Navier-Stokes (RANS) model and k-ε turbulence closure to simulate the mixing behavior of inclined dense jets. They reported some agreement of the numerical results compared to the laboratory measurements, however the terminal rise height was significantly underestimated. Oliver et al. (2008) also conducted a detailed numerical investigation of inclined dense jets using the RANS model. They concluded that the simulations provided a more accurate representation of the mixing processes for the inclined dense jet compared to the integral models. Gildeh et al. (2015) used the RANS model with different turbulence closures as well as the Reynolds Stress models (RSMs) (LRR and Launder–Gibson models) to simulate inclined dense jets. They concluded that RSMs generally yielded better results due to their ability to account for the anisotropic turbulence properties, but required more computational resources. More recently, Zhang et al. (2016) used the Large Eddy Simulations (LES) approach with both the Smagorinsky and dynamic Smagorinsky subgrid models to investigate the mixing behavior of 45° inclined dense jets. They showed that the simulations were able to reproduce the first order mixing characteristics of the inclined dense jet in a satisfactory manner. However, the dilution was underestimated which implied that some aspects of the turbulence mixing are not reproduced. Overall, the discrepancy in the predictions between the simulations and experiments in these studies demonstrated a need to further improve the understanding on the turbulence characteristics of the inclined dense jet. In particular, the study of the turbulent kinetic energy spectrum of the inclined dense jet will be useful in assessing the performance of the sub-grid models in LES so that more accurate simulations can be made in the future.

In the present study, we performed an extensive laboratory investigation to quantify the turbulence characteristics of 45° inclined dense jets using the PIV technique. The objective was to obtain benchmark data to guide high resolution numerical simulations for dense jets. The PIV measurements were sampled at a relatively high frequency of 50 Hz which enabled the resolution of the turbulence kinetic energy spectrum including the inertial subrange. Furthermore, we also performed numerical simulations using LES with the Dynamic Smagorinsky sub-grid model and GCI grid convergence criteria reported recently in Zhang et al. (2016, 2017), for the discharge conditions adopted in the laboratory experiments. In the following, we shall first describe the experimental setup, and then the details of the numerical simulations. Finally, a discussion of the comparison between the experimental and simulation results, with a focus on the turbulence kinetic energy spectrum, will be given.

2 Experimental setup

Experiments were performed in a towing flume with dimensions of 6.4 m (L) × 1.0 m (W) × 0.7 m (H) at the Environmental Hydraulic Laboratory at NEWRI. The experimental setup is shown schematically in Figure 2. The flume walls were made of transparent glasses for observation and measurements. The ceiling area above the water surface was masked with black cloth to eliminate the light reflection from the surface. A discharge nozzle, which was attached to a constant head tank, was placed on top of the flume. The constant head tank was elevated at 1.2 m above the nozzle to provide the driving pressure head for the dense jet discharge. The flow rate was controlled by a solenoid valve and measured by a flowmeter (Yokogawa AXF015G).

The experimental conditions are summarized in Table 1. A total of 13 experiments were performed with two nozzle diameters of 5.8 and 8.0 mm. The discharge velocities were sufficiently high so that the discharge Reynold Number exceeded 4000 and the jets were turbulent in all tests. The densities were varied in the different experiments and the Densimetric Froude Number ranged from 11 to 35. The density of the source saline water was determined by a density meter (Anton Paar, DMA 35N), and controlled to be 2.9% to 3.5% denser than the ambient water. The temperatures of both the ambient water and source solution were kept at 27.5 ± 1°C.

The PIV technique was used to measure the velocity field of the inclined dense jet. A dual-cavity pulsed laser (Dantec Dynamics, Class 4 Nd:Yag, DualPower 50-100 Laser, pulse repetition rate up to 50Hz) was installed below the transparent bottom for the generation of laser sheets. A high speed Charge-Coupled Device (CCD) digital camera (Dantec Dynamics, SpeedSense 1040) was used for image capturing in 8 bits grayscale with a maximum resolution of 2320 × 1726 pixels. It was typically set to double frame mode to synchronize with the dual-pulse laser, and its buffer size allowed a continuous acquisition of 25 s in full resolution. With this setup, the maximum laser pulsing frequency of 50Hz imposed the limiting constraint for the upper Nyquist frequency to be 25 Hz as discussed in Law and Wang (2000). The seeding particles were polyamide particles with a size of 50 μm.

For PIV, possible errors needed to be minimized at various stages of the measurement. The laser sheet should accurately penetrate the jet centerline plane and be carefully aligned with the jet discharge direction. A deviation of 1 mm between the jet center plane and laser sheet can cause a significant decrease in the values of the measured centerline velocity near the nozzle particularly with the small nozzle diameter of 5.8 mm in the experiments. Focusing the camera accurately was also found to be critically important for the turbulence measurements. Thus, before each experiment, the images were double checked to make sure that the particles in every interrogation window were clearly focused. In double frame mode, consecutive laser pulses were generated from two different laser sources. Therefore, the light intensities from the two laser pulses were also compared and aligned to ensure that the light intensity was almost equal between two consecutive images. In the present study, in order to further improve the accuracy as well as extend the time duration (number of images) for high quality second order turbulence statistics, the images were not recorded in full resolution but with decreased 1000 × 780 pixels, so that the image buffer could store continuously for a longer duration of about 100 seconds. As a result, only part of the dense jet can be captured in one image window with the actual physical size of 118 × 94 mm. Hence, the camera and laser were moved in a programmable manner to different locations during the experiment, until the composite images covered the entire trajectory of the inclined dense jet. For adaptive correlation analysis, the image was divided into interrogation areas (IAs). The smallest IA size was mainly determined by the requirement of having 5-15 seeding particles in each IA window (Law and Wang, 2000). In the present study, the image was divided based on 32 × 32 pixels IAs, with each IA having a physical size of ~3.8 × 3.8 mm. The time between two consecutive laser pulse was also different for different parts of the dense jet due to the different velocities. For the part of the dense jet with velocities faster than 1.0 m/s, the time between pulse of 800-1200 μs was used, while for velocities less than 1.0 m/s, 1200-

2500 μs was used instead. Finally, to reduce noise vectors, the algorithm of both “moving average validation” and "peak validation" were used during the adaptive-correlation analysis. Spurious vectors were removed when found, and replaced by the interpolation of three surrounding IAs. However, if the rejection percentage was high (exceeding 5%), we would repeat the measurements by varying the PIV parameters until the percentage became acceptable.

3 Results and discussion

3.1 Overall flow characteristics and jet trajectory

Figure 3 shows the contours of the time average velocities of the inclined dense jet from the experimental measurements with Fr = 15 and 30 (Tests F6 and F12, respectively). The centerline of the dense jet is plotted in the figure as a dashed line. From the contours, the discharge momentum dominated in the region near to the nozzle, and the behavior of the dense jet was jet-like with the velocity distribution nearly symmetrical about the centerline. Further downstream, the dense jet became asymmetrical with its lower half spreading wider due to the detrainment by the buoyancy induced instability (Kikkert et al. 2007, Papanicolaou et al. 2008, Crowe 2016b). We noted that the centerline trajectory of the inclined dense jet had been quantified in a number of previous studies (Shao and Law 2010, Lai and Lee 2012). The trajectories in the present study (Tests F6, F8, F11, F12 and F13) were normalized by FrD and plotted in Figure 4. From the figure, the normalized jet trajectories showed a general profile independent of Fr, which was in agreement with previous observation e.g. Shao and Law (2010).

3.2 Axial and cross-sectional turbulence intensity

The normalized turbulence intensity of the stream-wise velocity along the trajectory of the inclined dense jet is plotted along the axial distance from the nozzle in Figure 5 (for Tests F6, F9, F11, F12 and F13). It can be seen that the turbulence intensity decreased from the nozzle until approximately $0.4FrD$, and then began to increase reaching an averaged intensity of 0.3, which was close to the value of 0.27 obtained by Law and Wang (2000) for non-buoyant jets. This was consistent with the observation that the jet was momentum-dominated in the rising trajectory. Near the terminal rise location (which was approximately at $s = 2.0DFr$), the intensity decreased slightly. Figure 6 illustrates the turbulence intensity of the radial velocity along the centerline of the inclined dense jet in the same distance range. The intensity varied from 0.12 to 0.28 correspondingly. Figure 7 shows the cross-sectional distribution of the turbulence intensity (from Test F9). From the figure, the peak intensity appeared at the centreline, and the magnitude increased with the distance from the nozzle when $s/FrD < 1.5$. The cross-sectional profile was not axi-symmetric. The turbulence intensity at the lower half of the dense jet was relatively higher than the upper half, which can be attributed again to the buoyancy-induced instability.

3.3 Energy spectrum and Turbulence Kinetic Energy (TKE)

A total of 8 locations along the velocity centreline (x/FrD = 0.3, 0.5, 0.9, 1.2, 1.5, 1.8, 2.1 and 2.4) were selected for the spectral analysis. Their positions are shown in Figure 8. From Shao and Law (2000), the terminal rise of the 45° inclined dense jet occurs around $x/FrD = 1.7$. Hence, these eight locations included both the rising and falling stages of the inclined dense jet.

Figure 9 shows the turbulence kinetic energy spectrum at the centreline peak (Point 6) with different Fr (from Tests F6, F9, F11 and F12). Each energy spectrum was averaged from three repeated tests (100-120 seconds for each test). The inclined dense jet was driven by the upward discharge momentum to reach this location, and it was travelling primarily in the horizontal direction just before the excess buoyancy force drove it downward. From the figure, the magnitude at the lower frequency range ($f < 1$ Hz) of the spectrum increased with the discharge velocity U_o and thus Fr. This was consistent with the trend for the turbulence kinetic energy (TKE) as bulk of the turbulence energy should be contained in this production range. Comparatively, the influence was negligible for higher frequencies ($f > 1$ Hz). The measured spectrum exhibited the inertial subrange of −5/3 slope approximately from 2 Hz to 20 Hz, which was similar to the study for vertical buoyant jets by Papanicolaou (1984). There also appeared to be a correlation that the subrange began at a higher frequency with a lower Fr. At even higher frequencies (beyond 20 Hz), there were substantial noises due to the uncertainties of the PIV technique which led to a flattening white noise profile that was not physically meaningful (Foucaut et al. 2004).

Figure 10 shows the turbulence kinetic energy spectrum at the other locations from the nozzle (for Test F11, *Fr* = 25). From the figure, the spectral profile was flat at the two locations of Points 1 and 2 near to the nozzle, and the inertial subrange cannot be distinguished. This was attributed to the fact that the two points were inside the potential core of the dense jet. Thus, the production of turbulence kinetic energy by the Kelvin-Helmholz shear-induced eddies at the jet boundaries had not penetrated there yet. Similar conclusion was also drawn by Deshpande et al. (2009), which showed the appearance of inertial subrange delayed close to the nozzle due to the influence of the jet core.

The spectra at Points 3 and 4 showed the evolution of turbulence as the dense jet moved further away from the nozzle, with the slope for the inertial subrange progressively emerged. At Points 5 and 6 (centreline peak), the inertial subrange became clearly identifiable and spanned approximately from 2 to 20 Hz, which implied that the flow had reached the fully-developed state. It can also be observed that the spectral profile at lower frequencies increased slightly with the axial distance, which implied an increase in the turbulence energy production before the dense jet reached the centreline peak (Point 6). This observation was consistent with Fellouah and Pollard (2009) who measured for a turbulent round air jet. In the falling stage (Points 7 and 8), the turbulence energy production began to reduce and the magnitude of the spectral profile at the lower frequencies also decreased. At all locations, the limit of the turbulence kinetic energy spectrum was constrained by the temporal PIV frequency of 50 Hz and the corresponding Nyquist frequency of 25 Hz (Law and Wang, 2000) as discussed above. Thus, the spectral profile near and beyond 25Hz was unreliable and had a typical random noise-like behaviour.

4 Large Eddy Simulations

4.1 Previous LES modeling work on 45 °inclined dense jet

As discussed previously, Zhang et al. (2016, 2017) simulated the mixing of 45° inclined dense jets by means of the LES approach, with both the Smagorinsky and dynamic Smagorinsky sub-grid scale (SGS) models using GCI as the grid convergence criteria. Their analysis included the jet trajectory, jet spread, eddy structures and turbulence intensity. Their results showed that LES was able to predict the geometric characteristics of the inclined dense jet satisfactorily. At the same time, the dilution was underestimated, which was grossly attributed to the stratification effects on the convective mixing inside the sub-grids.

In the present study, the LES simulations were repeated for the specific discharge conditions as in the experiments using the dynamic Smagorinsky sub-grid scale (SGS) model and GCI grid convergence criteria. The details of the LES simulations are briefly given in the following. More details can be found in Zhang et al. (2016, 2017).

4.2 LES simulations

4.2.1 Governing equations

In the LES approach, eddies are filtered into large and small sizes based on the local sub-grid sizes. The relatively large energy-containing eddies with sizes bigger than the sub-grids are directly simulated by using the instantaneous Navier-Stokes equations, while the small eddies within the sub-grid are modeled by a sub-grid scale stress term. The filtered continuity, momentum and concentration transport equations in Cartesian coordinates (Pope 2002) for LES are shown from Eqs. (1) to (3), respectively:

$$\frac{\partial \bar{\rho}}{\partial t} + \frac{\partial}{\partial x_i}(\bar{\rho}\tilde{u}_i) = 0 \tag{1}$$

$$\frac{\partial(\bar{\rho}\tilde{u}_i)}{\partial t} + \frac{\partial}{\partial x_j}\left(\bar{\rho}\tilde{u}_i\tilde{u}_j\right) = -\frac{\partial \bar{p}}{\partial x_i} + \bar{\rho}g_i + \frac{\partial}{\partial x_j}\left(\mu\frac{\partial \tilde{u}_i}{\partial x_j}\right) - \frac{\partial \tau_{ij}}{\partial x_j} \tag{2}$$

$$\frac{\partial}{\partial t}(\bar{\rho}\tilde{\phi}) + \frac{\partial}{\partial x_j}(\bar{\rho}\tilde{\phi}\tilde{u}_j) = \frac{\partial}{\partial x_j}\left(\Gamma\frac{\partial\tilde{\phi}}{\partial x_j}\right) - \frac{\partial Q_j}{\partial x_j} \qquad (3)$$

where u_i, u_j are the velocity in i, j direction, respectively; ρ is the fluid density; p is the pressure; t is the time; g is the gravitational acceleration; μ is the fluid viscosity; Γ is the scalar diffusivity; ϕ is the scalar term; the overbar indicates time-averaged variables and the tilde indicates spatially filtered variables; $\tau_{ij} = \bar{\rho}\widetilde{u_i u_j} - \bar{\rho}\tilde{u}_i\tilde{u}_j$ are the SGS Reynolds stresses and $Q_j = \bar{\rho}\widetilde{\phi u_j} - \bar{\rho}\tilde{\phi}\tilde{u}_j$ are the SGS scalar flux.

The dynamic Smagorinsky SGS model is among the most popular in the existing SGS models so far (Dejoan and Leschziner 2005, Zhang et al. 2016). It represents the SGS stress tensor and SGS scalar flux in the format shown in Eqs. (5) and (6) respectively:

$$\tau_{ij} - \frac{1}{3}\tau_{kk}\delta_{ij} = -2\mu_t\tilde{S}_{ij} \qquad (4)$$

$$Q_j = -\frac{\mu_t}{Sc_t}\frac{\partial\tilde{\phi}}{\partial x_j} \qquad (5)$$

where τ_{kk} is the isotropic part of SGS stress which can be usually neglected for incompressible flows, Sc_t is the turbulent Schmidt number which can be varied but found to be ~0.7 (Yimer et al. 2002, Law 2006), and $\tilde{S}_{ij}$ is the rate of strain tensor for the resolved scale. μ_t is the SGS eddy viscosity, and Δ is the LES filter width. μ_t and $\tilde{S}_{ij}$ can be represented by the following equations:

$$\mu_t = \rho(C_S\Delta)^2|\tilde{S}| \qquad (6)$$

$$\tilde{S}_{ij} = \frac{1}{2}\left(\frac{\partial\tilde{u}_i}{\partial u_j} + \frac{\partial\tilde{u}_j}{\partial u_i}\right) \qquad (7)$$

C_S is determined by a localized dynamic procedure proposed by Germano et al. (1991) and further modified by Lilly (1992) as follow:

$$C_S^2 = \frac{\langle L_{ij}M_{ij}\rangle}{2\langle M_{ij}M_{ij}\rangle} \qquad (8)$$

$$L_{ij} = \widehat{\tilde{u}_i\tilde{u}_j} - \hat{\tilde{u}}_i\hat{\tilde{u}}_j \qquad (9)$$

$$M_{ij} = \Delta^2\widehat{|\tilde{S}|\tilde{S}_{ij}} - \hat{\Delta}^2\left|\hat{\tilde{S}}\right|\hat{\tilde{S}}_{ij} \qquad (10)$$

where the angular brackets indicate a spatial averaging procedure over directions of statistical homogeneity, and the caret indicates a spatial filtered quantity on the test-filter. For calculating the scalar transport, the following equations were further developed (Lilly, 1992).

$$Sc_t = \frac{C_S^2}{C_\phi^2} \tag{11}$$

$$C_\phi^2 = \frac{\langle \varepsilon_j R_j \rangle}{\langle R_j R_j \rangle} \tag{12}$$

$$\varepsilon_j = \widehat{\tilde{u}_j \tilde{\phi}} - \hat{\tilde{u}}_j \hat{\tilde{\phi}} \tag{13}$$

$$R_j = \Delta^2 \widehat{|\tilde{S}| \frac{\partial \tilde{\phi}}{\partial x_j}} - \hat{\Delta}^2 \left|\hat{\tilde{S}}\right| \frac{\partial \hat{\tilde{\phi}}}{\partial x_j} \tag{14}$$

4.2.2 Numerical setup

In the present study, the equations were discretized using the finite volume method, and simulations were performed using the open source CFD package OpenFOAM (Jasak 2009). The implementation of the governing equations in OpenFOAM was carried out with the turbulence solver, twoLiquidMixingFoam. It is a standard solver for the mixture flow of two incompressible fluids, and has been used and validated in many studies (Gruber et al. 2011, Lai et al. 2015 and Zhang et al. 2016).

4.2.3 Physical parameters

To evaluate the grid convergence, a series of mesh scheme were configured and tested for simulating the first order average characteristics first. After that, the selected grids were further tested for simulating the turbulence characteristics of the inclined dense jet. The numerical conditions for the simulations cases are listed in Table 2. The fluid viscosity and diffusivity were 10^{-6} kg•m^{-1}s^{-1} and 10^{-9} m^2/s, respectively. The density of ambient water was 997.3 to 998.5 kg/m^3, and two port diameters of 5.8 and 8.0 mm were used. The numerical conditions were identical to the physical parameters used in the experiments.

4.2.4 Computational domain

Figure 11 shows a schematic diagram of the computational domain, where the origin of Cartesian coordinates was set to the center of the discharge nozzle. The distances from the port to the back (L_1), front (L_2), left (W_2) and right sides (W_1), and surface (H) boundaries for each case were always larger than 1*DFr*, 8*DFr*, 4*DFr*, 4*DFr* and 4*DFr*, respectively, to ensure sufficient clearance to resolve the dense jet under full submergence (Jiang et al. 2014). The distance to the bottom boundary (h) was larger than 1*DFr*, which was sufficient to avoid the Coanda effect (Shao and Law, 2010).

4.2.5 Computing conditions

The boundary condition at the top surface of the computational domain was set to free slip, while a zero gradient open boundary was used for the left, right, bottom, back and front boundaries. The nozzle opening was set as a velocity inlet with a uniform discharge velocity and a turbulence intensity of 5-10%. The corresponding dense fluid density was specified in Table 1. The other surfaces of the discharge tube were set to be wall boundaries. A second order implicit backward scheme was used for the discretization of the temporal term. An upwind and a linear scheme were used to compute the divergence term and the Laplacian term, respectively. The convergence criterion of 10^{-6} was set for the velocities simulation.

4.2.6 Computing hardware

The simulations were performed with parallel computing at the High Performance Computing Centre at the Nanyang Technological University. The calculations of each case were decomposed using the technique of domain decomposition and computed with parallel executions using 16 or 96 CPU cores. The time of simulation duration, t_s, from the beginning of the simulated discharge was from 60s to 130s to ensure the flow was fully-developed and had reached steady state. For most of the LES simulations, the real-time computing duration ranged from 8-18 days as shown in Table 2.

4.2.7 Grid scheme

The computational domain was discretized with a stretched and structured mesh with increasing grid spacing from the center of the nozzle to the boundaries. In addition, a double refinement was performed within the region that covered the potential core of the dense jet. The grids attached to the discharge tube were generated by the snappyHexMesh tool in openFOAM, which can divide a base structured cell into several sub-cells and then snap the sub-cell boundaries onto the surface of the discharge tube.

In theory, if the LES grid spacing is sufficiently small into the inertial subrange, the sub-grid model would then be able to represent the turbulence within the cell in an almost exact manner. In the present conditions, however, the Kolmogorov length scale was estimated to be about 2.4×10^{-5} m. This requirement was too demanding with respect to the computing resources available to this study. Thus, similar to Zhang et al. (2016), the method of Grid Convergence Index (GCI) (Celik et al. 2008) was used instead for the gross grid convergence. The first order key parameters selected for GCI evaluation were the centreline peak velocity and centreline peak height of the inclined dense jet. In addition, the effect of grid size for the simulation of the turbulence spectrum beyond GCI was also examined through different mesh schemes. Three different meshes with the minimum grid spacing of 3.0×10^{-3}, 2.2×10^{-3} and 1.1×10^{-3} m were used, the grid spacing of the mesh was increasing from the centre of the port to the boundaries. In particular, a double refinement was performed within a region that covered the core of the jet, as shown in Figure 12. The corresponding grid numbers were 8, 10 and 16 million, respectively (shown in Table 2). The numerical conditions were as follow. Cases N1A and N1B simulated experimental Test F1 (Fr = 11, D = 8mm) by using two different grid spacing with grid numbers of 8 and 10 million, respectively. Case N6A simulated the Test F6 (Fr = 15, D = 5.8mm) with grid number of 16 million. Cases N9A, N9B and N9C simulated Test F9 (Fr = 20, D = 5.8mm) with 8, 10 and 16 million, respectively, and Cases N11A and N11B simulated Test F11 (Fr = 25, D = 5.8mm) with 10 and 16 million, respectively. Finally, Case N12A simulated Test F12 (Fr = 30, D = 5.8mm) with the grid number of 16 million.

4.2.8 Overall flow characteristics and jet trajectory

Figure 13 shows the mean velocity contours from experimental Test F6 and numerical Case N6A. The centerlines are plotted as black dashed lines in the figure. The simulated behavior was in general agreement with the experiment as mentioned before, with the jet-like stage in the region near to the nozzle. The flow field was symmetrical about the centerline in the region near to the nozzle, and became asymmetrical further downstream due to the buoyancy induced instability. The simulated velocity magnitudes in Figure 13(b) were also close to the experimental results.

Figure 14 shows the normalized jet trajectories for both the experiments (Tests F6, F9, F11, F12 and F13) and simulations (Cases N1B, N9B, N11B, N12A). From the figure, the trajectories showed a general profile independent of *Fr*, which was consistent with previous observation e.g. Shao and Law (2010). However, the centerline peak height was lower than the numerical results of the linear eddy viscosity models (RNG k-ε and realizable k-ε models) and Reynolds stress models (LRR and Launder-Gibson models) reported by Gildeh et al. (2015). It also can be observed that the centerline peak height from the nonlinear eddy viscosity model (nonlinear k-ε model) was much larger than the results from LES as well as experiments. Upstream of the centerline peak, the simulated trajectories by LES agreed well with the experimental results. Beyond that, the rise height from LES simulation was slightly larger than the experimental results, but was still within the range of experimental data observed previously.

4.2.9 Velocity decay

The velocity decay along the centerline was determined from both the experimental and numerical results. Previously, Chen and Rodi (1980) suggested a power law relationship for vertical buoyant jets between the non-dimensional centerline dilution and distance from the nozzle as follow:

$$Fr.C_m/C_0=a(z/D/Fr)^b \tag{15}$$

where a and b are constants dependent on whether the flow is in the jet-like, transition, or plume-like regime. Shao and Law (2010) observed a similar relationship for the velocity decay between FrU_m/U_0 and $s/D/Fr$ for the inclined dense jet, where s is the axial distance along the centerline. The variations of the normalized maximum centerline velocity and normalized downstream distance are presented in Figure 15, where the axes are in a logarithmic scale. s was calculated in a discretized manner both for the experiments (Tests F1, F6, F7, F9 and F11) and numerical simulations (Cases N1B, N9C). As seen from the figure, the numerical results followed the experimental data reasonably well. The transition regime can be observed approximately at $1.0 < s/D/Fr < 8$. Moving away from the nozzle, i.e. $s/D/Fr > 1.0$, the data points collapsed on a curve with the relationship of $FrU_m/U_0 = 4.8(s/D/Fr)^{-1.1}$, which was consistent with the observation reported by Shao and Law (2010). Nevertheless, it should be noted that the larger exponent on the right hand side beyond 1.0 indicated the early effect of buoyancy on the jet-like range.

4.2.10 Velocity fluctuations

Figure 16 shows the velocity fluctuations at the centerline peak (Point 6) for the Experimental Test F1 and Numerical Cases N1A and N1B. The time average velocity was close to 0.11 m/s for both. However, N1A had a relatively coarse grid with a total grid number of 6 million, and the magnitude of velocity fluctuations was much smaller than what was measured in the experiments as shown in the figure. Thus, although both N1A and N1B satisfied the GCI criteria in terms of convergence for the first order parameters, the turbulence intensities for N1A were grossly underestimated. Comparatively, the magnitude of the velocity fluctuations in N1B using a finer grid scheme was much closer to the experimental results. Therefore, simulation results from N1A and N9A which had the coarse grid were not presented in the following discussion. This demonstrated that further examination of turbulence details is necessary in order to achieve satisfactory predictions on turbulence mixing characteristics.

4.2.11 Cross-sectional velocity profile

The cross-sectional distributions of the normalized average stream-wise velocity (U/U_m) are plotted in Figure 17 at four different locations ($s/\mathrm{Fr}D$ = 0.4, 0.8, 1.2 and 1.6 respectively) along the centerline (for Test F11 and Case N11B, $Fr = 25$). In the figure, the upper and lower halves of the inclined dense jet are represented by negative and positive values of r/D, respectively. Again, it can be observed that near to the nozzle (e.g. sFr/D = 0.4), the velocity profiles were symmetrical and followed the Gaussian distribution. Further downstream, the spread of the lower half became wider. The asymmetry increased with $s/\mathrm{Fr}D$, and the profile deviated from the Gaussian curve progressively. The behavior was again repeated in Figure 18 (Tests F1, F6, F9, F11 and Cases N1B, N6A, N9C, N11B) whereby the normalized stream-wise velocity is plotted with different normalized values of s/DFr. Overall, the simulated results can be seen to be in good agreement with the experimental data.

The normalized 1/e widths for the upper half of the dense jet (defined as where the velocity decreases to e^{-1} of the centerline maximum value in the cross-section) from the experiments (Tests F1, F6, F7, F9, F11 and F12) and simulations (Cases N9C, N11B and N12A) are shown in Figures 19 and 20. Generally, the 1/e width increased linearly with the stream-wise distance as had been commonly reported in previous studies (Lai and Lee 2012, Crowe 2016a). However, in Figure 20, the lower half of the dense jet can be observed to grow markedly faster than the upper half (~0.14 for the upper half and 0.36 for the lower half). The numerical results were close to the experimental results for the upper half, but much lower for the lower half where the buoyancy induced instability creates turbulence production in high frequencies. However, resolving the high frequencies required much smaller grid spacing, which beyond the available computational resources at present.

4.2.12 Axial and cross-sectional turbulence intensity

The simulated (Cases N9C, N11B and N12A) stream-wise turbulence intensity along the centerline trajectory is plotted in Figure 21. The stream-wise intensity increased until $s = 1.5FrD$ and began to decrease after that. The simulated intensities were slightly lower than the experimental results (Tests F6, F9, F11, F12 and F13). Figure 22 illustrates the simulated radial intensity along the trajectory in the same spatial range. The radial intensity varied from 0.12-0.20 with an average of 0.15, which was close to the experimental results.

In Figure 23, the turbulence intensity profile at the centerline peak is compared between Experimental Test F9 and Numerical Case N9C. At this location, the simulated turbulence intensity was lower in the upper and particularly the lower half where the buoyancy-induced instability was present. Again, both the experimental and numerical results showed that the cross-sectional distribution of turbulence was not axis-symmetric. The intensity in the lower half was obviously larger than the upper half when $s > 1.5FrD$. Closer to the nozzle when $s = 0.5FrD$ and $1.0FrD$, double peaking of turbulence intensity can be clearly observed from the simulated profile. On the contrary, the distribution was uniform in the central region of the inclined dense jet from the experimental measurements. This direct comparison implied that the magnitude of turbulence inside the dense jet was higher in the experiment which led to stronger lateral mixing that diminished the distribution peaks.

4.2.13 Turbulence kinetic energy spectrum and Turbulence Kinetic Energy (TKE)

Figure 24 shows the comparison of spectra at the centreline peak for Experiment Test F12 and Numerical Cases N12A and N12B. The difference between the simulated energy spectra for Cases N12A and N12B was small, yet it can be clearly observed that N12B with the finer grids yielded higher turbulence energy production before the inertial subrange. The numerical and experimental spectra had similar magnitude at the lower frequencies representing the main production range approximately up to ~1 Hz. Thus, the results implied that the present LES simulations can efficiently resolve bulk of the turbulence kinetic energy for the inclined dense jet. However, the simulated spectral profiles dropped off much faster compared to the experiments towards the higher frequencies, with the inertial subrange showing up much earlier in the lower frequencies for both N1A and N1B. Thus, the additional turbulence energy production in this transitional range which was obviously present in the physical tests, was not fully reproduced in the LES simulations.

The stream-wise turbulence kinetic energy spectrum at the different locations are shown in Figure 25 for Experimental Test F9 and Numerical Case N9C ($Fr = 20$), and also Figure 26 for Test F12 and Case N12B ($Fr = 30$). Earlier, we had discussed that the experimental spectral profiles at Points 1 and 2 were relatively flat which can be attributed to the presence of the potential core. This can also be seen in the numerically simulated spectra up to about ~1 Hz (i.e. below the sub-grid modeling frequency), but not for higher frequencies. The likely reason was that the LES simulation had assumed sub-grid turbulence characteristics following the Dynamic Smargorinsky model, which was not strictly applicable for this potential core region. From Points 1 to 8, the simulated spectrum decreased with the log slope which was approximate -5/3 between the frequency of 2 to 20Hz. Subsequently, the predicted spectrum decreased much faster at higher frequencies. The magnitude of the turbulence energy density simulated by LES at low frequencies (less than 1Hz) was close to the experimental results. However, the simulated turbulence energy density failed to capture the energy production between ~1 to 3 Hz before the start of the inertial subrange. We believe that the main source of this transitional energy production was due to stratified effects within the sub-grid, particularly the convective overturning due to the buoyancy induced instability at the lower half of the inclined dense jet. Comparing Figs 24 and 25, the agreement between experimental and LES results improved, which was consistent with the expectation that the transitional turbulence production due to buoyancy induced instability played a lesser role in Test F12 with higher U_o and thus Fr which would be more jet-like. Further refining the grid spacing and increasing the grid number beyond 16 million was not possible in this study due to the constraint in computational resources and budget. We note that our constraint is already at the higher end of what would be typically available to engineering companies to validate their final design at the moment.

5 Conclusion

An experimental investigation was performed to quantify the turbulence characteristics of 45° inclined dense jets using the PIV technique. The objective was to provide benchmark data to guide high resolution turbulence simulations of dense jets in the future. The PIV measurements were taken at a high sampling frequency so as to resolve the turbulence kinetic energy spectrum at different locations along the jet trajectory (which was identified using the time-averaged velocity field). The average velocity of the inclined dense jet generally decayed with the stream-wise distance of s following the relationship of $FrU_m/U_0=4.8(s/D/Fr)^{-1.1}$ after $s/Fr/D > 1.0$. The experimental turbulence kinetic energy spectrum decreased with the log slope of -5/3 at the frequency from ~2 to 20Hz near and beyond the centreline peak. LES simulations with different mesh schemes were also conducted. The simulated turbulence kinetic energy spectrum was close to experimental results for lower frequencies (from 0.01-1.0Hz), however the transitional energy production beyond ~1 Hz and before the inertial subrange was not reproduced satisfactorily in the simulations due to the minimum grid spacing adopted. In summary, the present results demonstrated that the evolution of the turbulence characteristics for 45 degree inclined dense jet along the trajectory is complex, and thus the numerical modelling of the mixing behaviour is challenging. The LES simulations performed in this study was able to reproduce the first order dense jet mixing characteristics and also a large part of the turbulence spectrum at the production range when proper sub-grid model and grid size were selected. However, the results also show that further improvement in terms of sub-grid models that can incorporate the stratification effects is necessary for engineering simulations in the future.

Acknowledgement

The authors would like to thank the Nanyang Environment & Water Research Institute and the Interdisciplinary Graduate School at Nanyang Technological University, for the award of research scholarship to the first author.

References

Celik, I. B., U. Ghia and P. J. Roache (2008). "Procedure for estimation and reporting of uncertainty due to discretization in CFD applications." Journal of Fluids Engineering **130**(7): 078001

Chen, C. J. and W. Rodi (1980). "Vertical turbulent buoyant jets: a review of experimental data." NASA STI/Recon Technical Report A 80

Christodoulou, G. C. and I. G. Papakonstantis (2010). "Simplified estimates of trajectory of inclined negatively buoyant jets." Proceedings of the 6th International Symposium on Environmental Hydraulics **1**:165-170.

Christodoulou, G. C., I. G. Papakonstantis and I. K. Nikiforakis (2015). "Desalination brine disposal by means of negatively buoyant jets." Desalination and Water Treatment **53**(12): 3208-3213.

Cipollina, A., A. Brucato, F. Grisafi and S. Nicosia (2005). "Bench-scale investigation of inclined dense jets." Journal of Hydraulic Engineering, ASCE **131**(11): 1017-1022.

Crowe, A. T., M. J. Davidson and R. I. Nokes (2016a) "Velocity measurements in inclined negatively buoyant jets." Environmental Fluid Mechanics **16**(3): 503-520.

Crowe, A. T., M. J. Davidson and R. I. Nokes (2016b). "Modified reduced buoyancy flux model for desalination discharges." Desalination **378**: 53-59.

Dejoan, A. and M. A. Leschziner (2005). "Large eddy simulation of a plane turbulent wall jet." Physics of Fluids **17**(2): 025102.

Drami, D., Y. Z. Yacobi, N. Stambler and N. Kress (2011). "Seawater quality and microbial communities at a desalination plant marine outfall. A field study at the Israeli Mediterranean coast." Water Research **45**(17): 5449-5462.

Deshpande, S. S., M. J. Sathe and J. B. Joshi (2009). "Evaluation of local turbulence energy dissipation rate using PIV in jet loop reactor." Industrial and Engineering Chemistry Research **48**(10): 5046-5057.

Fellouah, H. and A. Pollard (2009). "The velocity spectra and turbulence length scale distributions in the near to intermediate regions of a round free turbulent jet." Physics of Fluids **21**(11): 115101.

Foucaut, J. M., J. Carlier and M. Stanislas (2004). "PIV optimization for the study of turbulent flow using spectral analysis." Measurement Science and Technology **14**(6): 1046-1058.

Germano, M., U. Piomelli, P. Moin and W. H. Cabot (1991). "A dynamic subgrid ‐ scale eddy viscosity model." Physics of Fluids A: Fluid Dynamics **3**(7): 1760-1765.

Gildeh, H. K., A. Mohammadian, I. Nistor and H. Qiblawey (2015). "Numerical modeling of 30 degrees and 45 degrees inclined dense turbulent jets in stationary ambient." Environmental Fluid Mechanics **15**(3): 537-562.

Gruber, M. F., C. J. Johnson, C. Y. Tang, M. H. Jensen, L. Yde and C. Hélix-Nielsen (2011). "Computational fluid dynamics simulations of flow and concentration polarization in forward osmosis membrane systems." Journal of Membrane Science **379**(1-2): 488-495.

Heisenberg, W. (1948). "On the theory of statistical and isotropic turbulence." Proceedings of the Royal Society of London A **195**(1042): 402-406.

Jasak, H. (2009). "OpenFOAM: open source CFD in research and industry."International Journal of Naval Architecture and Ocean Engineering **1**(2): 89-94.

Jiang, B., A. W. K. Law and J. H. W. Lee (2014). "Mixing of 30 and 45 inclined dense jets in shallow coastal waters." Journal of hydraulic engineering**140**(3): 241-253.

Kikkert, G. A., M. J. Davidson and R. I. Nokes (2007). "Inclined negatively buoyant discharges." Journal of Hydraulic Engineering, ASCE **133**(5): 545-554.

Kolmogorov, A. N. (1941). "The local structure of turbulence in incompressible viscous fluid for very large Reynolds numbers." Dokl. Akad. Nauk SSSR **30**: 9–13.

Lai, C. C. and J. H. Lee (2012). "Mixing of inclined dense jets in stationary ambient." Journal of Hydro-Environment Research **6**(1): 9-28.

Lai, A. C., B. Zhao, A. W. K. Law and E. E. Adams (2015). "A numerical and analytical study of the effect of aspect ratio on the behavior of a round thermal." Environmental Fluid Mechanics **15**(1): 85-108.

Law, A. W. K. and H. Wang (2000). "Measurement of mixing processes with combined digital particle image velocimetry and planar laser induced fluorescence." Experimental Thermal and Fluid Science **22**(3): 213-229.

Law, A. W. K. (2006). "Velocity and concentration distributions of round and plane turbulent jets." Journal of Engineering Mathematics **56**(1): 69-78

Lilly, D. K. (1992). "A proposed modification of the germano-subgrid-scale closure method." Physics of Fluids A-Fluid Dynamics **4**(3): 633-635.

Milione, M. and C. Zeng (2008). "The effects of temperature and salinity on population growth and egg hatching success of the tropical calanoid copepod, Acartia sinjiensis." Aquaculture **275**(1): 116-123.

Obukhov, A. (1941). "Spectral energy distribution in a turbulent flow." Izv. Akad. Nauk. SSSR. Ser. Geogr. i. Geofiz **5**: 453-466.

Oliver, C. J., M. J. Davidson and R. I. Nokes (2008). "k-ε Simulations of the initial mixing of desalination discharges." Environmental Fluid Mechanics **8**(5-6): 617-625.

Palomar, P., J. L. Lara, I. J. Losada, M. Rodrigo and A. Alvarez (2012). "Near field brine discharge modelling part 1: Analysis of commercial tools." Desalination **290**: 14-27.

Papakonstantis, I. G., G. C. Christodoulou and P. N. Papanicolaou (2011a). Inclined negatively buoyant jets 1: Geometrical characteristics. Journal of Hydraulic Research 49 (1): 3-12

Papakonstantis, I. G., G. C. Christodoulou and P. N. Papanicolaou (2011b). "Inclined negatively buoyant jets 2: concentration measurements." Journal of Hydraulic Research **49**(1): 13-22.

Papanicolaou, P. N. (1984). "Mass and momentum transport in a turbulent buoyant vertical axisymmetric jet." (Doctoral dissertation, California Institute of Technology).

Papanicolaou, P. N., I. G. Papakonstantis and G. C. Christodoulou (2008). "On the entrainment coefficient in negatively buoyant jets." Journal of Fluid Mechanics **614**: 447-470.

Pope, S. (2002). "Turbulent Flow." Cambridge University Press, Cambridge, U.K.

Roberts, P. J. W. and G. Toms (1987). "Inclined Dense Jets in Flowing Current." Journal of Hydraulic Engineering **113**(3): 323-341.

Roberts, P. J. W., A. Ferrier and G. Daviero (1997). "Mixing in inclined dense jets." Journal of Hydraulic Engineering **123**(8): 693-699.

Shao, D. and A. W. K. Law (2010). "Mixing and boundary interactions of 30° and 45° inclined dense jets." Environmental Fluid Mechanics **10**(5): 521-553.

Vafeiadou, P., I. G. Papakonstantis and G. C. Christodoulou (2005). "Numerical simulation of inclined negatively buoyant jets." Proceedings, 9th International Conference on Environmental Science and Technology: A1537–A1542.

Wang, H. and A. W. K. Law (2002). "Second-order integral model for a round turbulent buoyant jet." Journal of Fluid Mechanics **459**: 397-428.

Westerweel, J., G. E. Elsinga and R. J. Adrian (2013). “Particle Image Velocimetry for Complex and Turbulent Flows.” Annual Review of Fluid Mechanics, **45**:409-436.

Yimer, I., I. Campbell and L. Y. Jiang (2002). "Estimation of the turbulent Schmidt number from experimental profiles of axial velocity and concentration for high-Reynolds-number jet flows." Canadian Aeronautics and Space Journal **48**(3): 195-200.

Zhang, S., B. Jiang, A. W. K. Law and B. Zhao (2016). "Large eddy simulations of 45° inclined dense jets." Environmental Fluid Mechanics **16**(1): 101-121.

Zhang, S., A. W. K. Law and M. Jiang (2017). "Large eddy simulations of 45° and 60° inclined dense jets with bottom impact." Journal of Hydro-Environment Research **15**: 54-66.

List of Symbols

b_e	Velocity 1/e width
C_0	Initial concentration
C_m	Centerline concentration
C_s	Smagorinsky constant
D	Nozzle diameter
Fr	Densimetric Froude number
g	Gravitational acceleration
g'	Reduced gravitational acceleration
h	Port height
H	Distance from the port to the water surface
L	Distance from the port to the back and front vertical boundary
L_M	Jet characteristic length scale
L_{ij}	Resolved turbulent stress
M_{ij}	Anisotropic part of the turbulent stress
p	Pressure
Q_j	SGS scalar flux or turbulent scalar flux
r	Radial distance
Re	Reynolds number
s	Stream-wise distance from the nozzle
$\tilde{S}$	Local strain rate
$Sc_t = 0.7$	Turbulent Schmidt number
S_{ij}	Rate of strain tensor for the resolved scale
t	Time
t_s	Run time of a simulation
U	Stream-wise velocity
U'	Fluctuation of stream-wise velocity
U_0	Discharge velocity
U_m	Jet velocity along the centerline
U'_{rms}	Root mean square stream-wise velocity fluctuation

u_i, u_j	Velocity in i, j direction, respectively
u_τ	Friction velocity
V	Radial velocity
V'	Fluctuation of radial velocity
V'_{rms}	Root mean square radial velocity fluctuation
W	Distance from the nozzle to the left and right vertical boundary
x, y, z	Cartesian Coordinates in the horizontal, lateral and vertical direction, respectively
x_m	Horizontal location of centerline peak
Δ	LES filter width
ρ	Fluid density
ρ_a	Ambient density
ρ_b	Effluent density
μ	Fluid viscosity
μ_t	SGS eddy viscosity or turbulent eddy viscosity
ϕ	Scalar concentration
ε	Dissipation rate
τ_{ij}	SGS Reynolds stresses or Reynolds stresses
τ_{kk}	Isotropic part of SGS stress
Γ	Scalar diffusivity
Γ_t	Turbulent dispersivity

List of Figures

Figure 1 Schematic diagram of an inclined dense jet discharged into stagnant ambient (side view)
Figure 2 Experimental setup of this tudy
Figure 3 Time averaged velocity field of the inclined dense jet: (a) Test F6, *Fr* = 15 (b) Test F12, *Fr* = 30
Figure 4 Measured normalized jet trajectories of the 45° inclined dense jets
Figure 5 Turbulence intensity of stream-wise velocity along the jet centerline
Figure 6 Turbulence intensity of radial velocity along the jet centerline
Figure 7 Cross-sectional distribution of stream-wise turbulence intensity (Test F9)
Figure 8 Locations for analysis of the turbulence kinetic energy spectrum
Figure 9 Experimental turbulence kinetic energy spectrum at centerline peak with different *Fr*
Figure 10 Experimental turbulence kinetic energy spectrum at different locations (Test F11)
Figure 11 Computational domain of the LES simulations
Figure 12 Mesh for LES simulation (N9C)
Figure 13 Instantaneous horizontal velocity field: (a) Test F6 and (b) Case N6A
Figure 14 Normalized trajectories of inclined 45° dense jets
Figure 15 Comparison of velocity decay along the jet centerline
Figure 16 Instantaneous velocity fluctuation at Point 6
Figure 17 Cross-sectional distribution of stream-wise velocity along the trajectory (Test F11 and Case N11B)
Figure 18 Cross-sectional distribution of radial velocity along the jet trajectory
Figure 19 Variation of upper 1/e width along the jet trajectory
Figure 20 Variation of lower 1/e width along the jet trajectory
Figure 21 Variation of stream-wise turbulence intensity along the jet trajectory
Figure 22 Variation of radial turbulence intensity along the jet trajectory
Figure 23 Cross-sectional distribution of stream-wise turbulence intensity along the jet trajectory
Figure 24 Turbulence kinetic energy spectrum at centerline peak

Figure 25 Turbulence kinetic energy spectrum at different locations along the trajectory (Test F9 and Case N9C)

Figure 26 Turbulence kinetic energy spectrum at different locations along the trajectory (Test F12 and Case N12B)

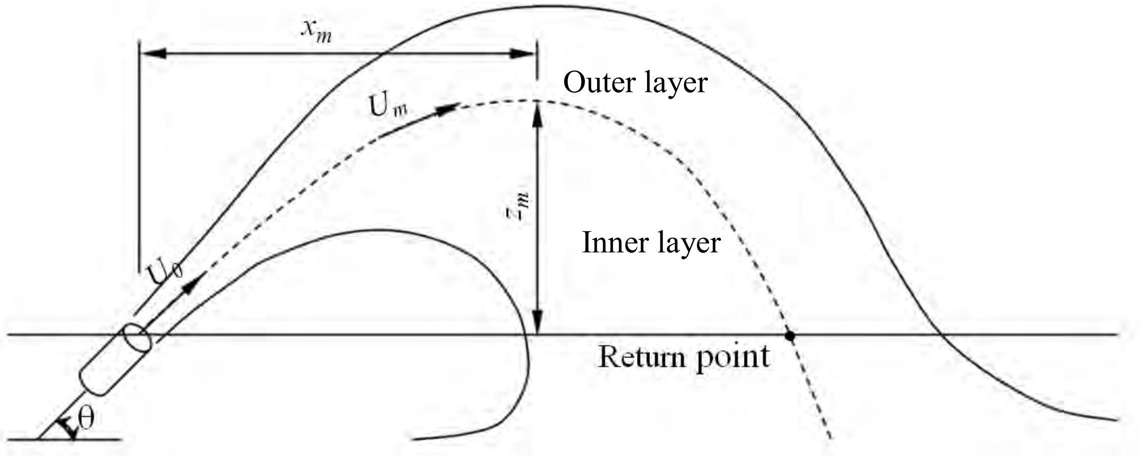

Figure 1

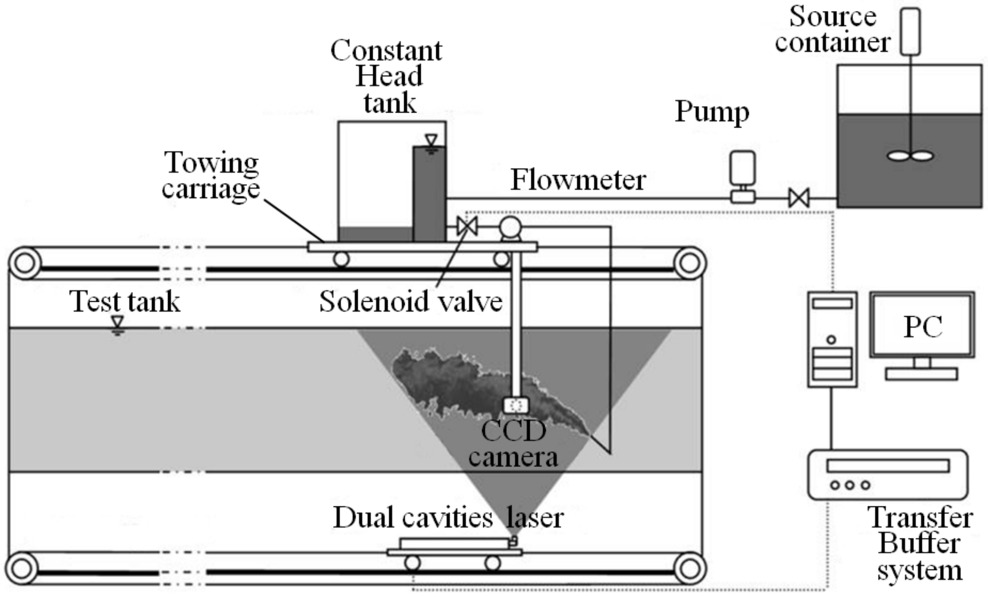

Figure 2

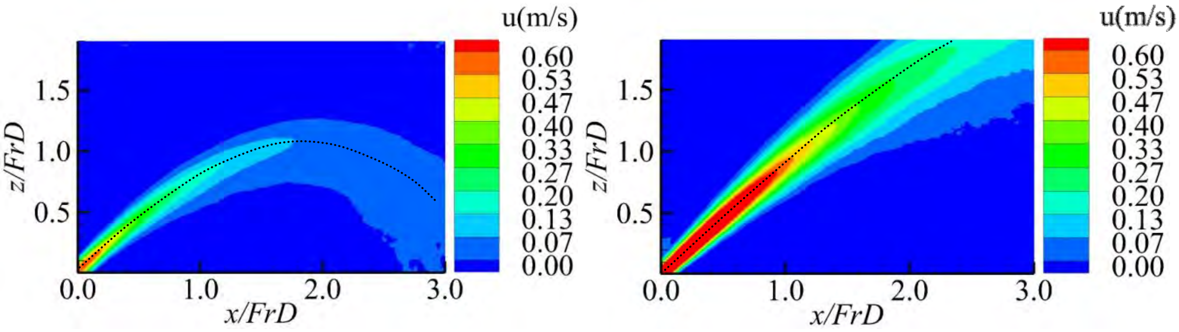

(a) (b)

Figure 3

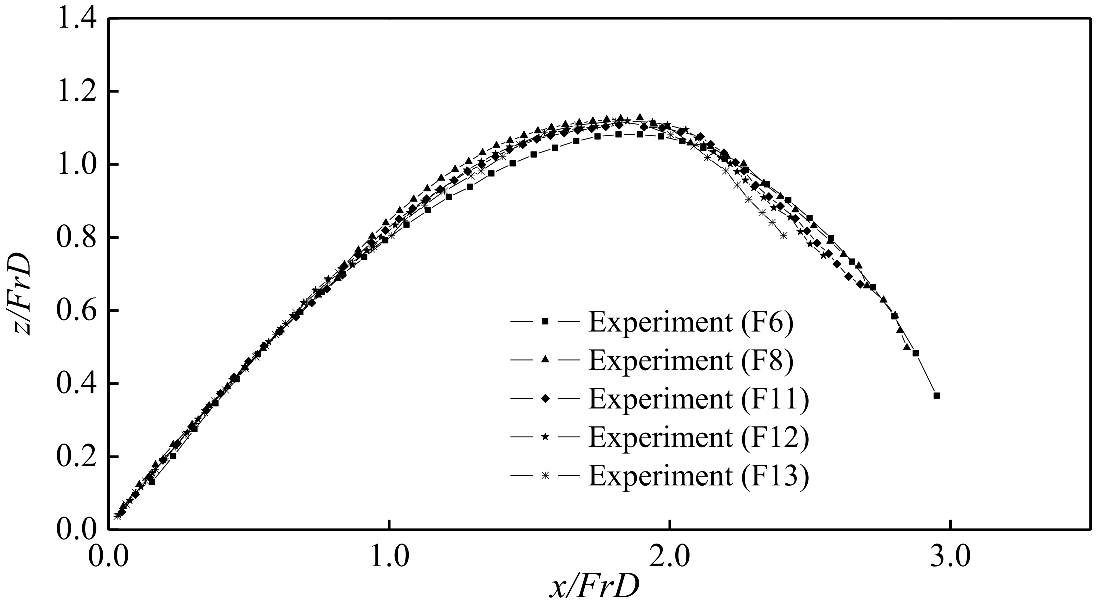

Figure 4

732

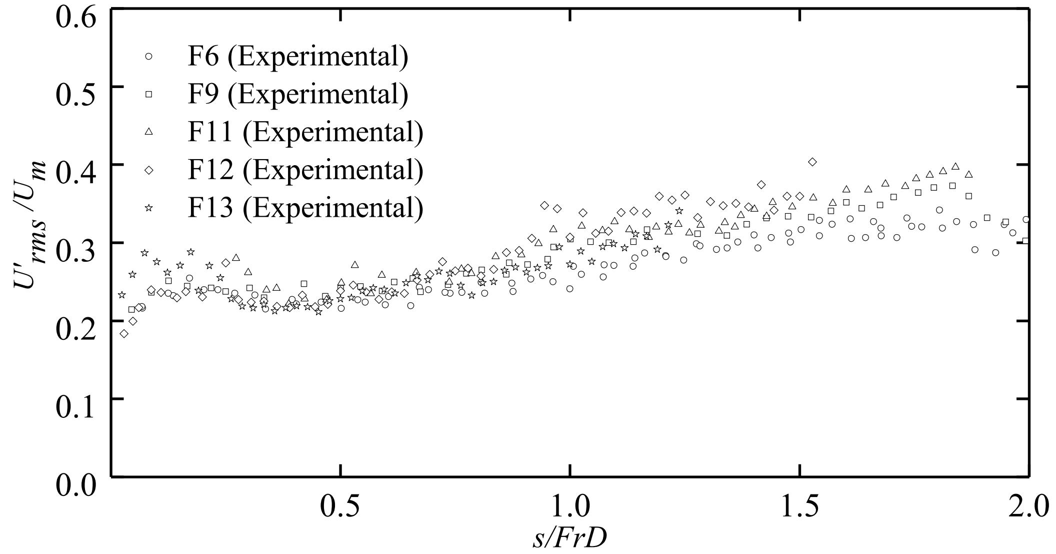

733 Figure 5

734

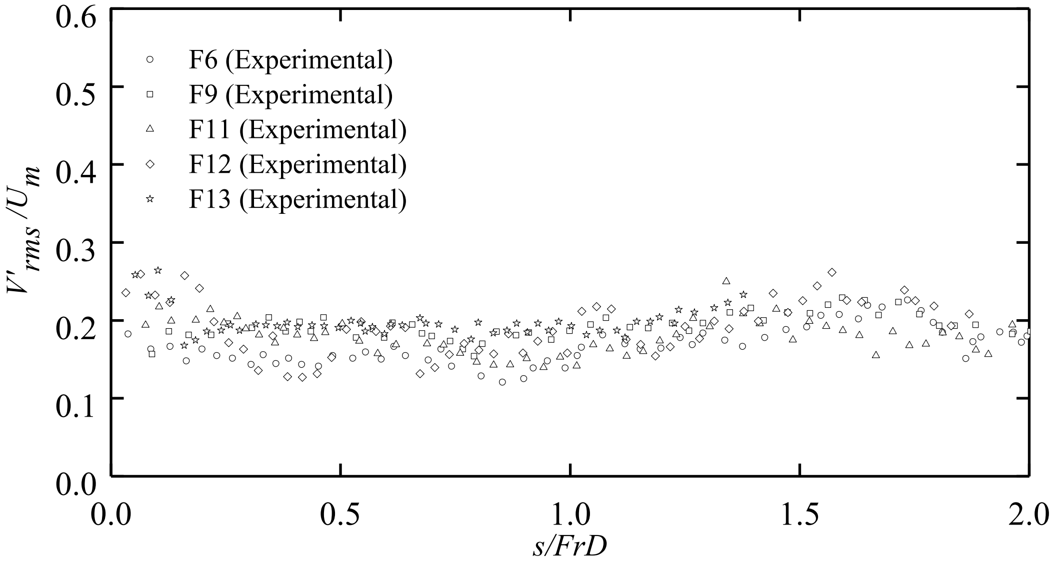

735

736 Figure 6

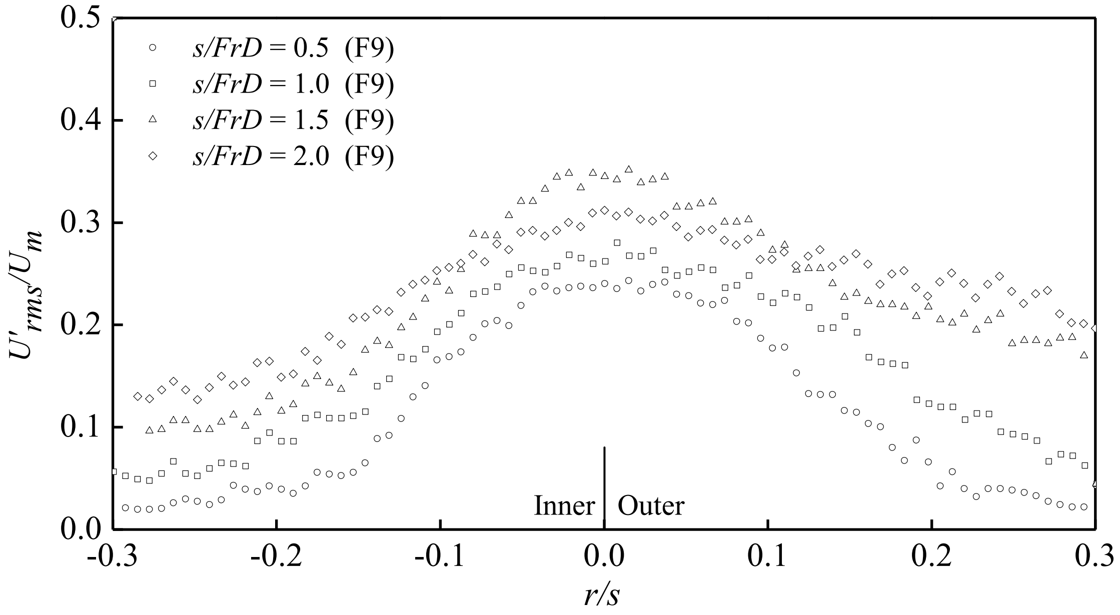

s/FrD = 0.5 (F9)
s/FrD = 1.0 (F9)
s/FrD = 1.5 (F9)
s/FrD = 2.0 (F9)
U'rms/Um
r/s
Inner
Outer
0.0
0.1
0.2
0.3
0.4
0.5
-0.3
-0.2
-0.1
0.0
0.1
0.2
0.3

Figure 7

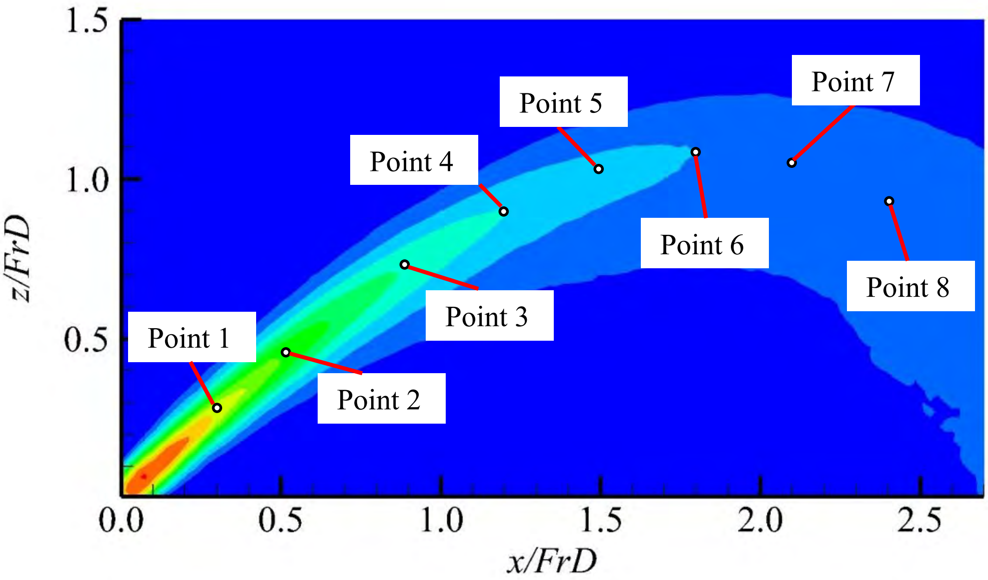
Point 1
Point 2
Point 3
Point 4
Point 5
Point 6
Point 7
Point 8
z/FrD
x/FrD
1.5
1.0
0.5
0.0
0.5
1.0
1.5
2.0
2.5

Figure 8

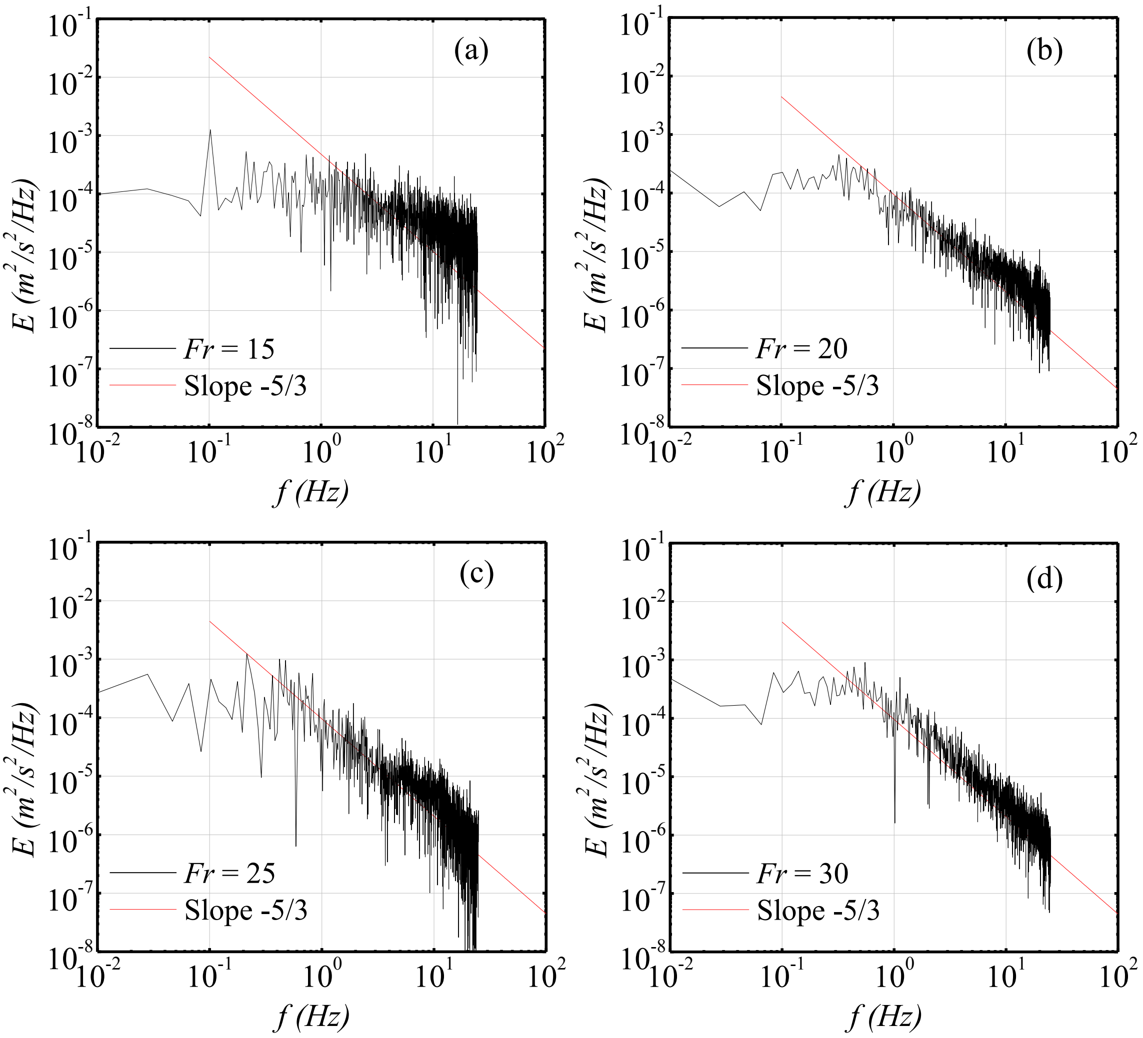
(a)
(b)
(c)
(d)
$E\ (m^2/s^2/Hz)$
$f\ (Hz)$
10^{-1}
10^{-2}
10^{-3}
10^{-4}
10^{-5}
10^{-6}
10^{-7}
10^{-8}
10^{0}
10^{1}
10^{2}
Fr = 15
Fr = 20
Fr = 25
Fr = 30
Slope -5/3

Figure 9

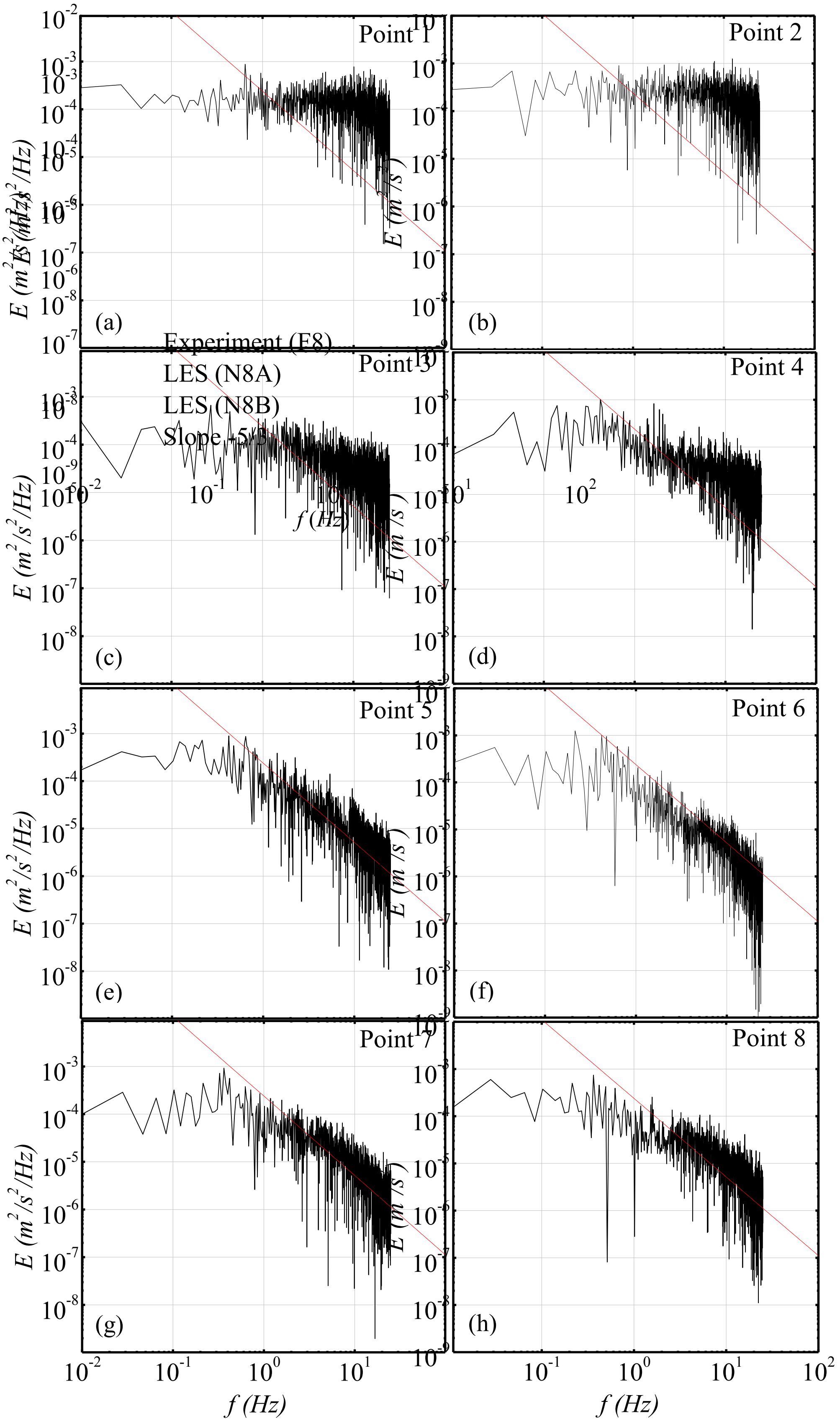
Point 1
Point 2
Point 3
Point 4
Point 5
Point 6
Point 7
Point 8
(a)
(b)
(c)
(d)
(e)
(f)
(g)
(h)
Experiment (F8)
LES (N8A)
LES (N8B)
Slope -5/3
$E\ (m^2/s^2/Hz)$
10^{-3}
10^{-4}
10^{-5}
10^{-6}
10^{-7}
10^{-8}
10^{-2}
10^{-1}
10^{0}
10^{1}
10^{2}
$f\ (Hz)$

Figure 10

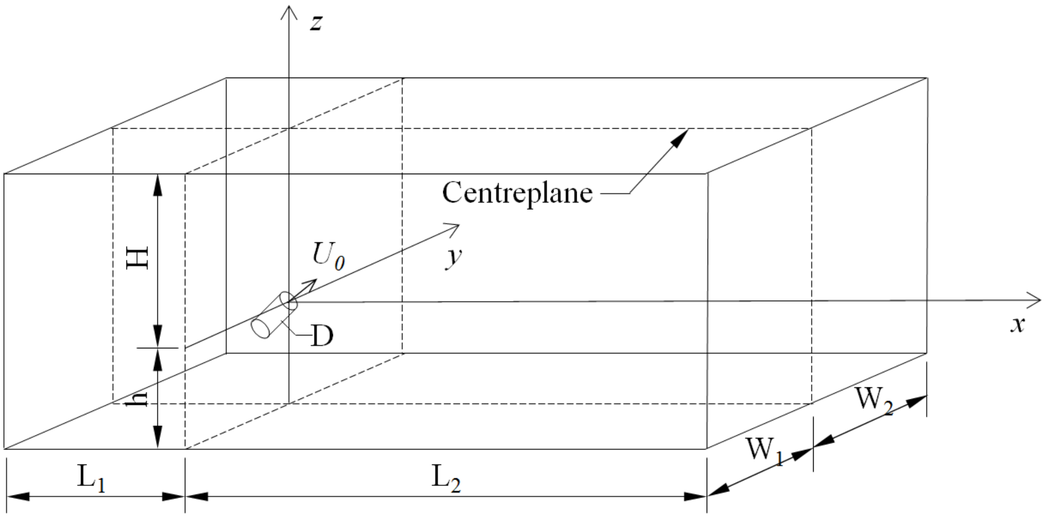

Figure 11

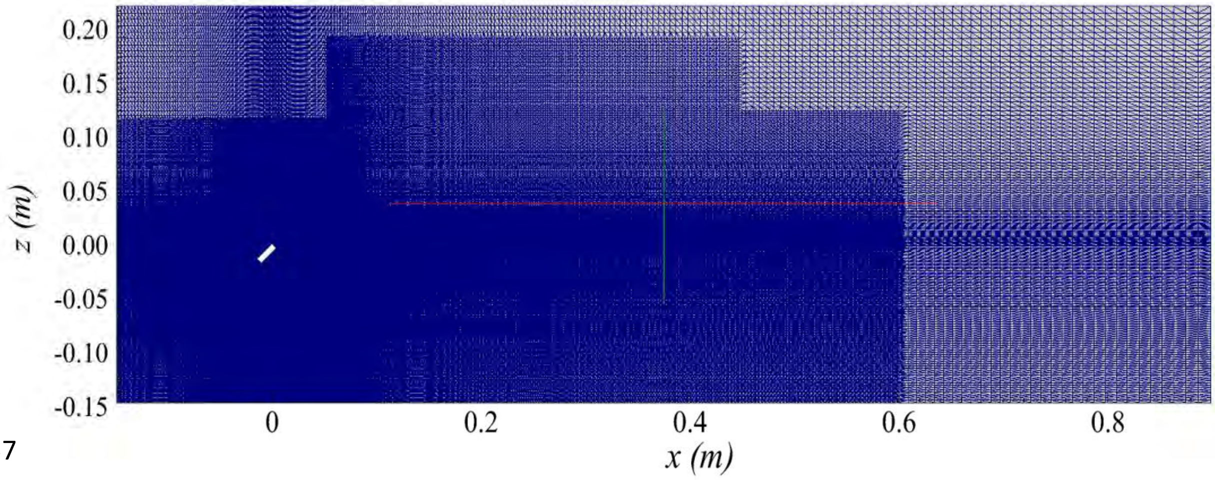

(a) Plane View

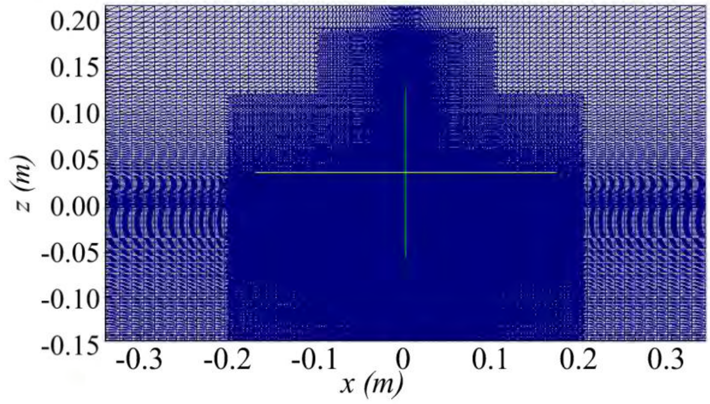

(b) Section view

Figure 12

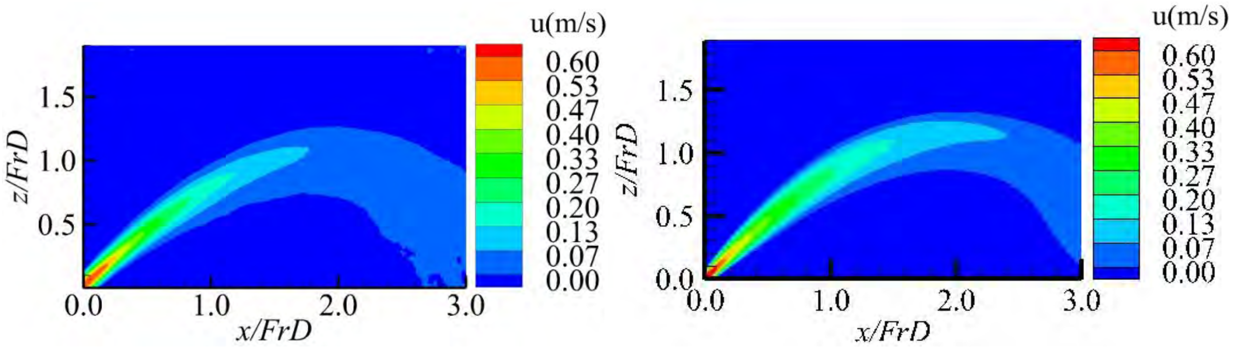

(a) (b)

Figure 13

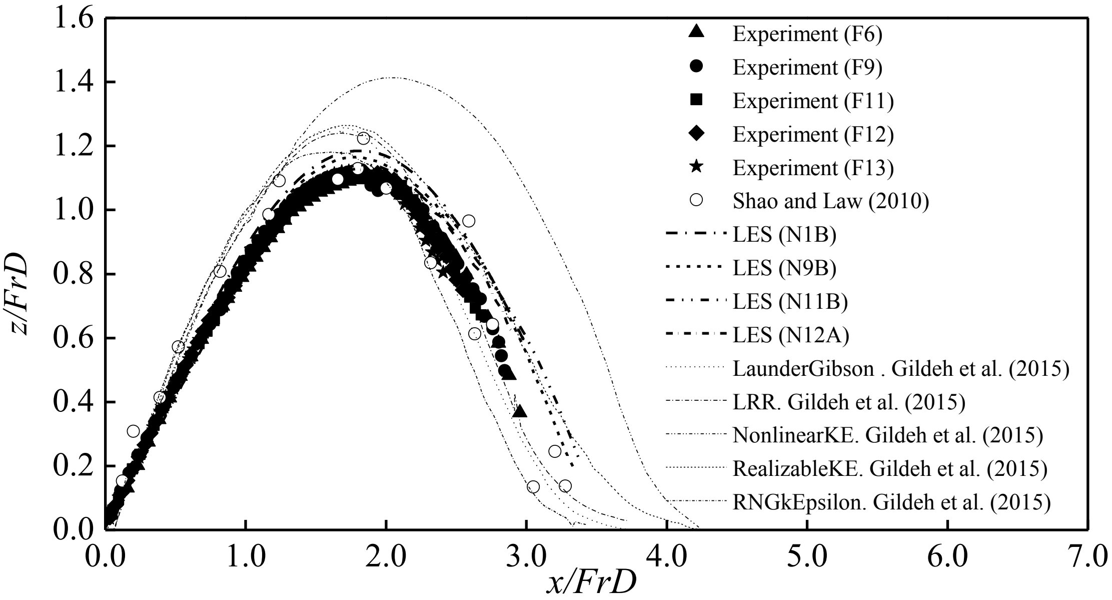

Figure 14

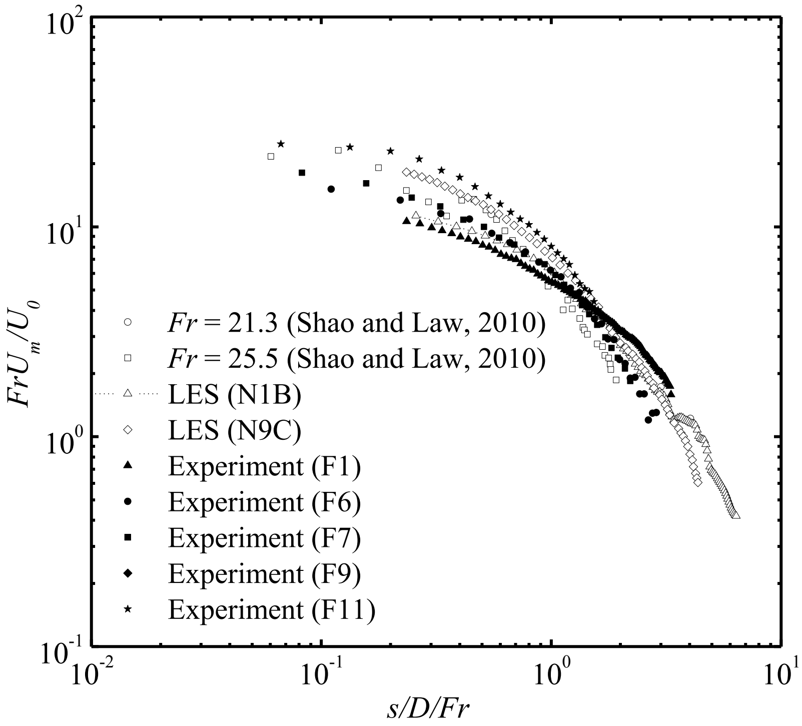

Figure 15

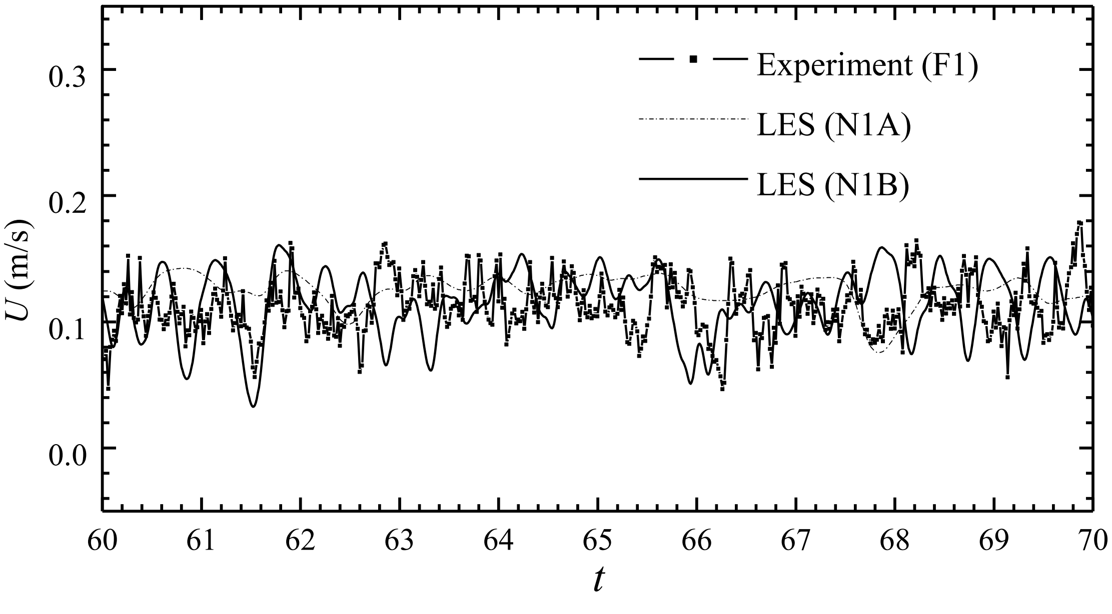

Figure 16

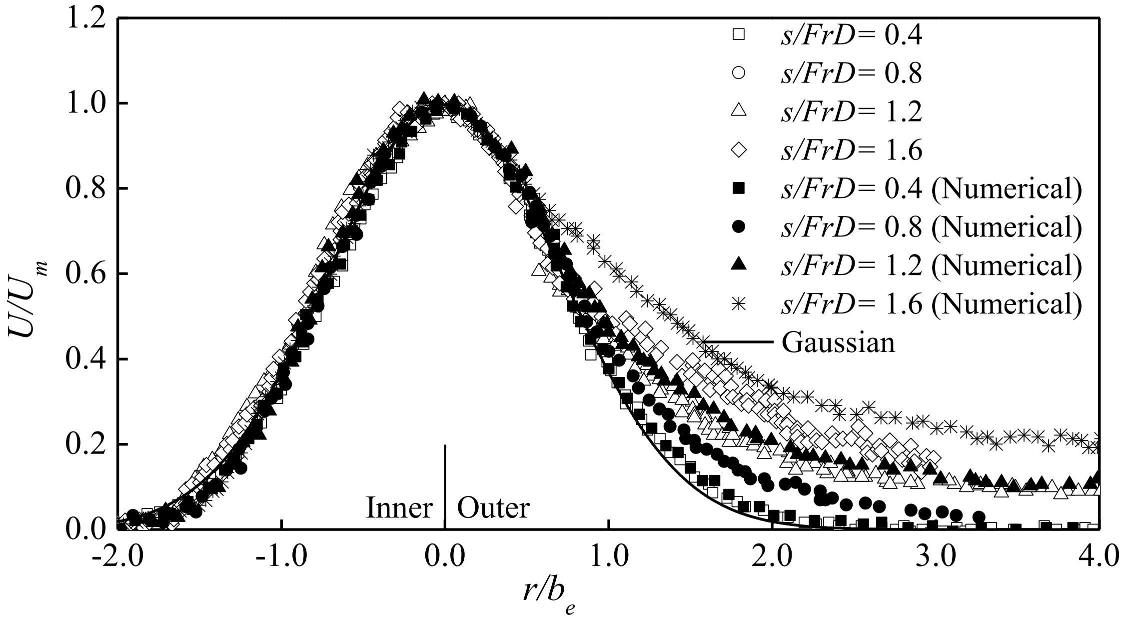

Figure 17

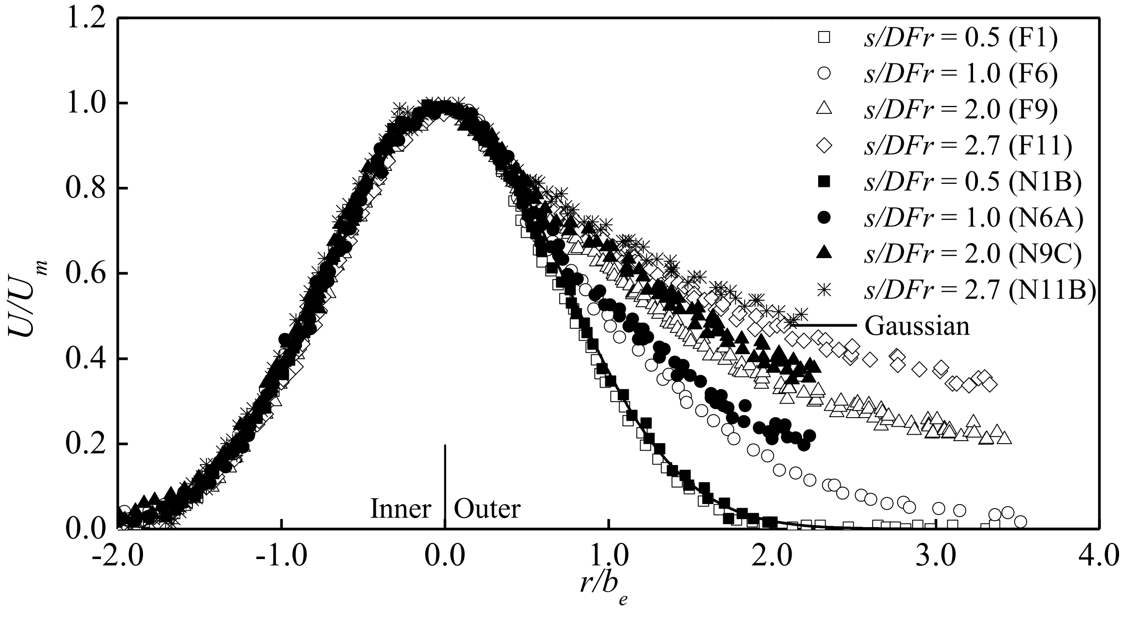

Figure 18

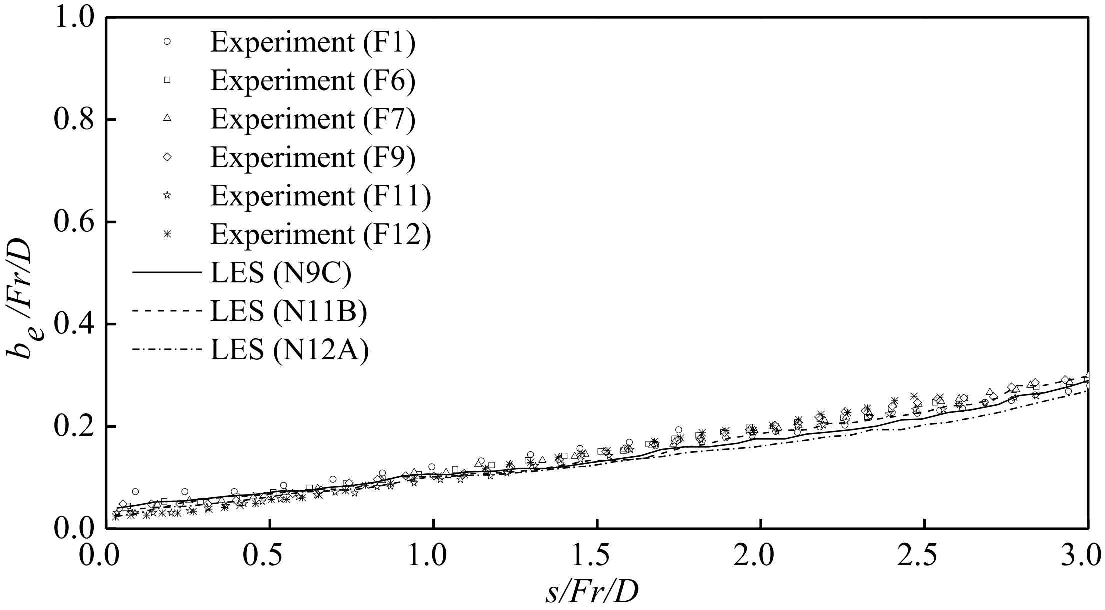

Figure 19

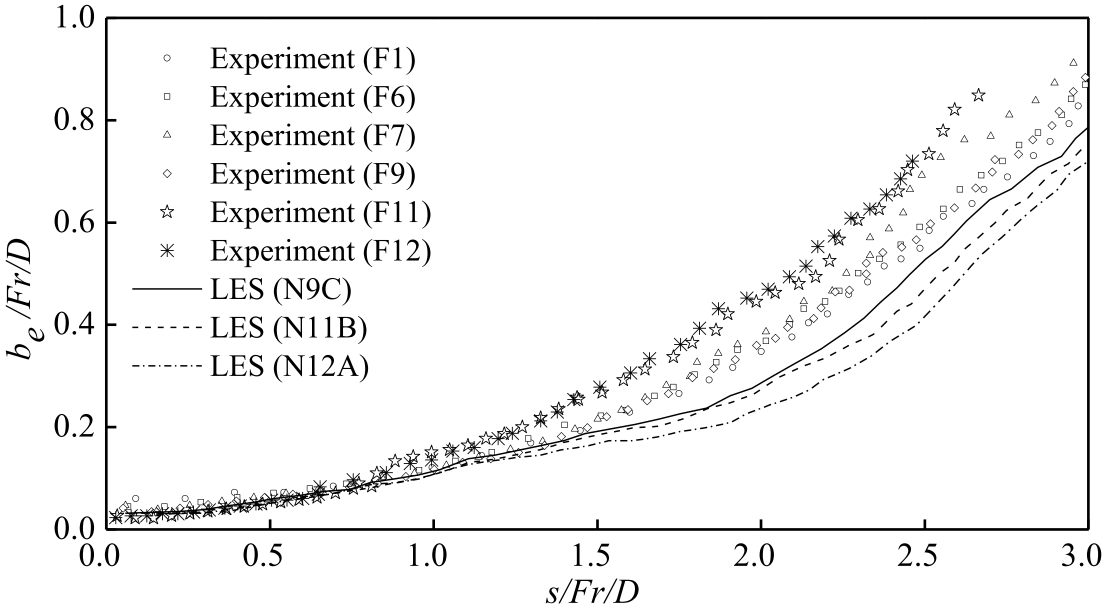

Figure 20

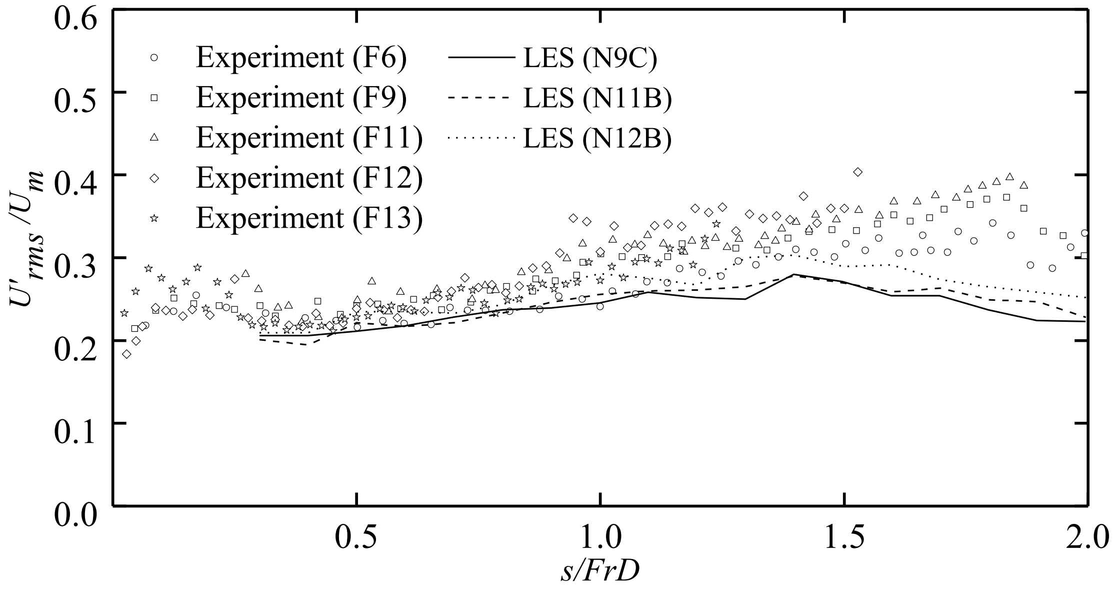

Figure 21

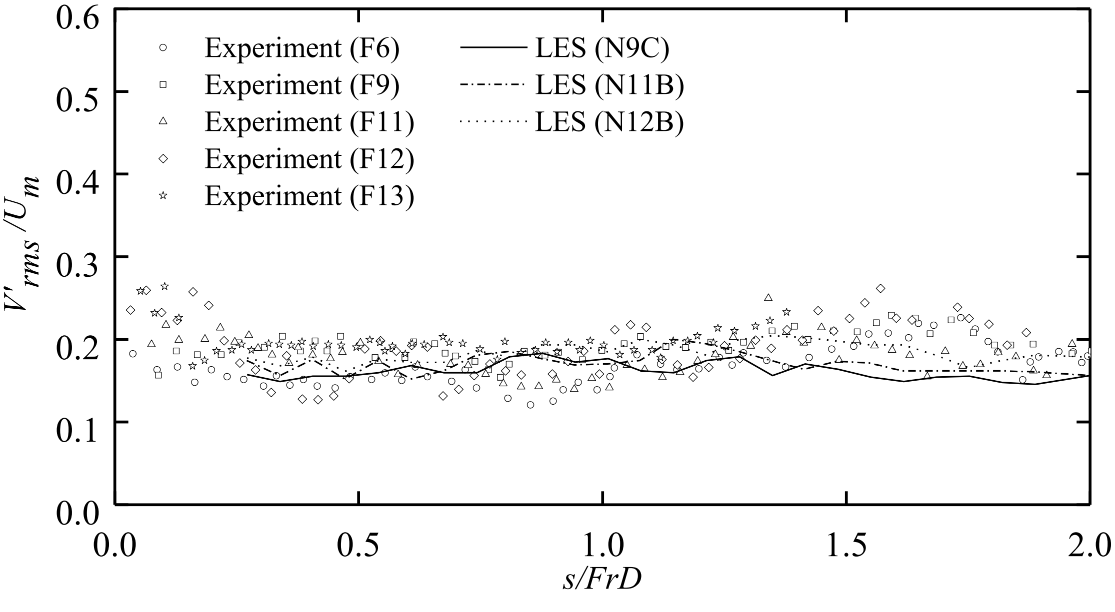

Figure 22

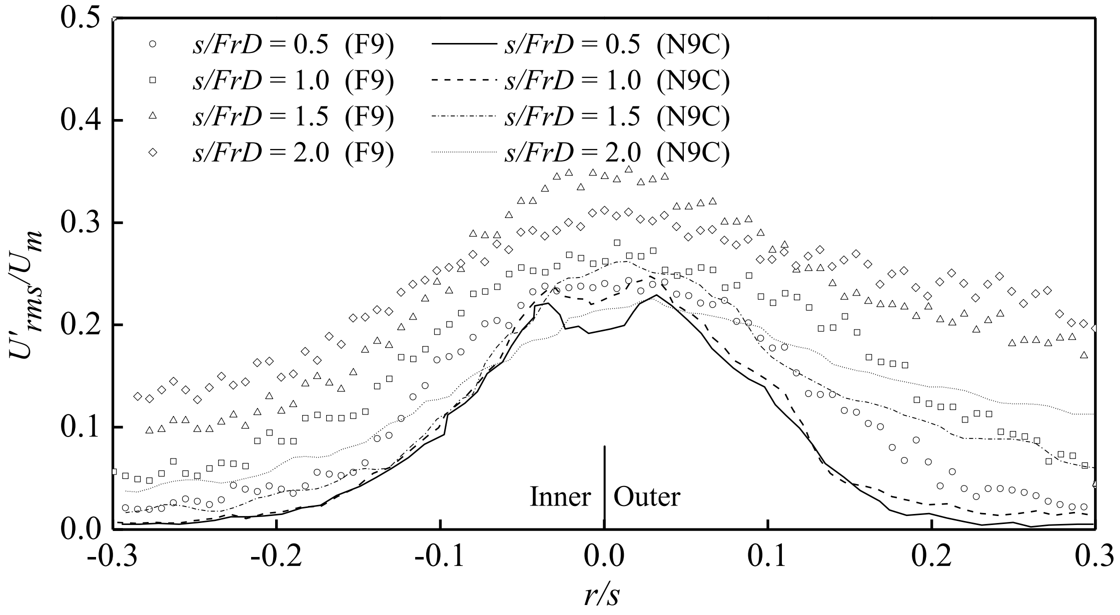

Figure 23

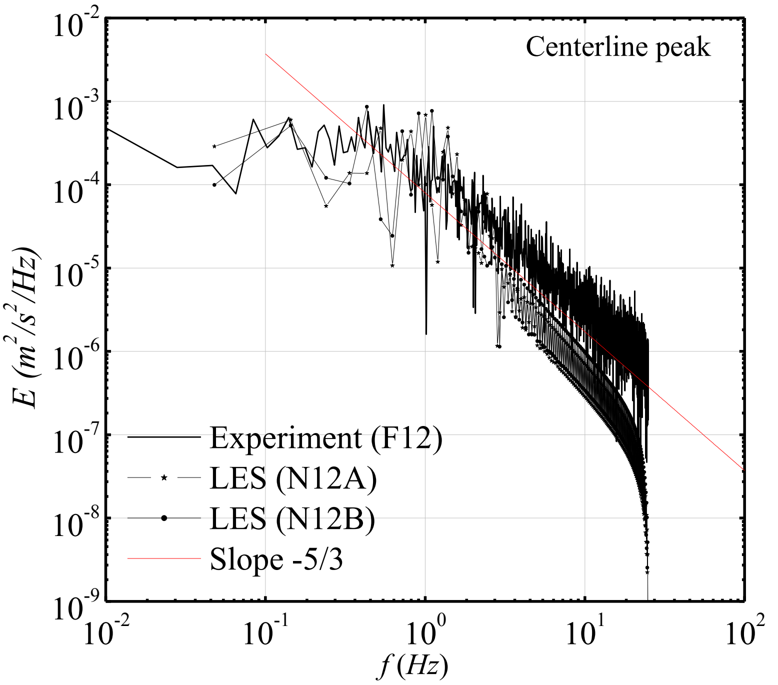

Figure 24

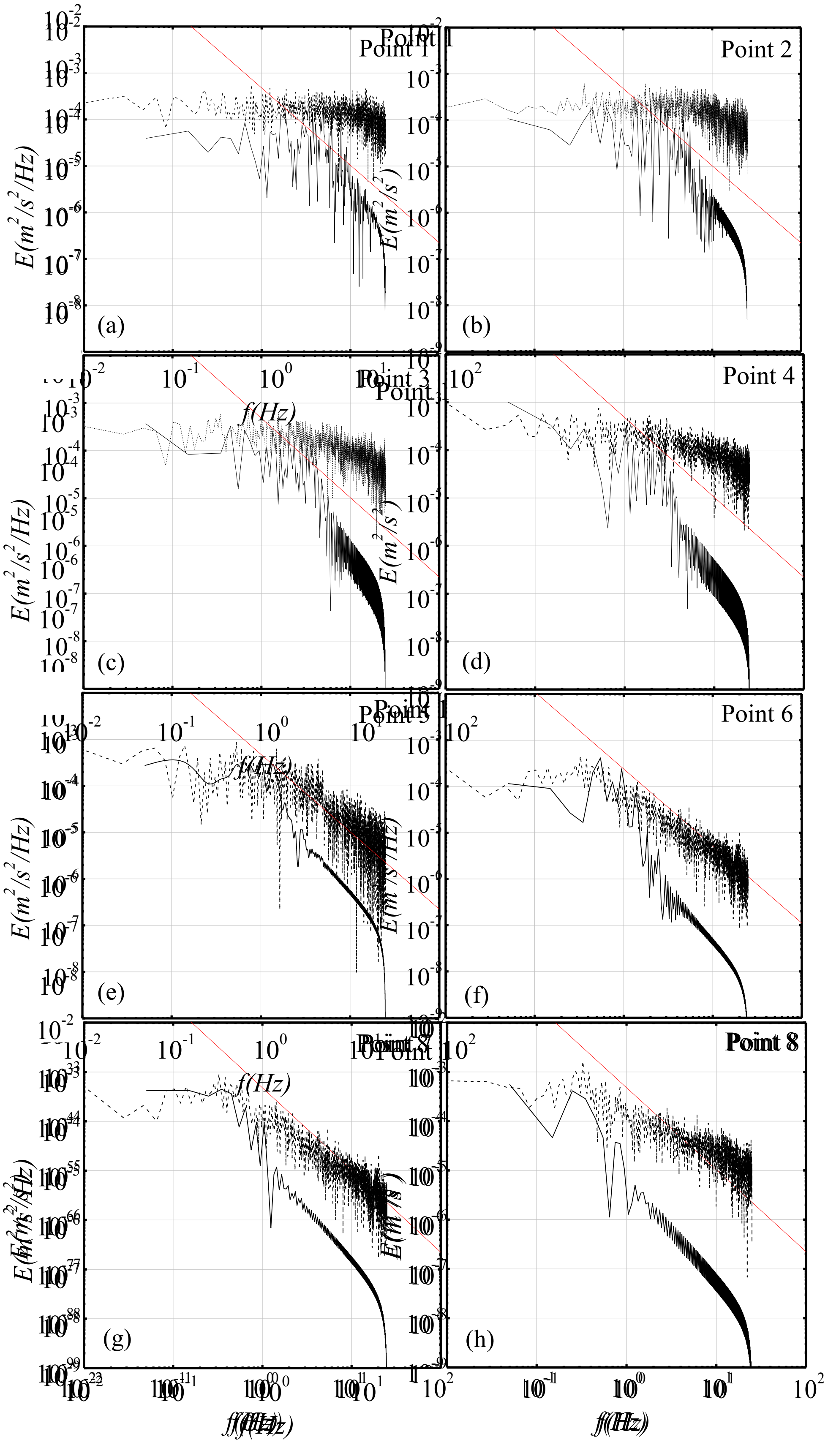
Point 1
Point 2
Point 3
Point 4
Point 5
Point 6
Point 7
Point 8
(a)
(b)
(c)
(d)
(e)
(f)
(g)
(h)
$E(m^2/s^2/Hz)$
$f(Hz)$
10^{-2}
10^{-3}
10^{-4}
10^{-5}
10^{-6}
10^{-7}
10^{-8}
10^{-9}
10^{-1}
10^{0}
10^{1}
10^{2}

Figure 25

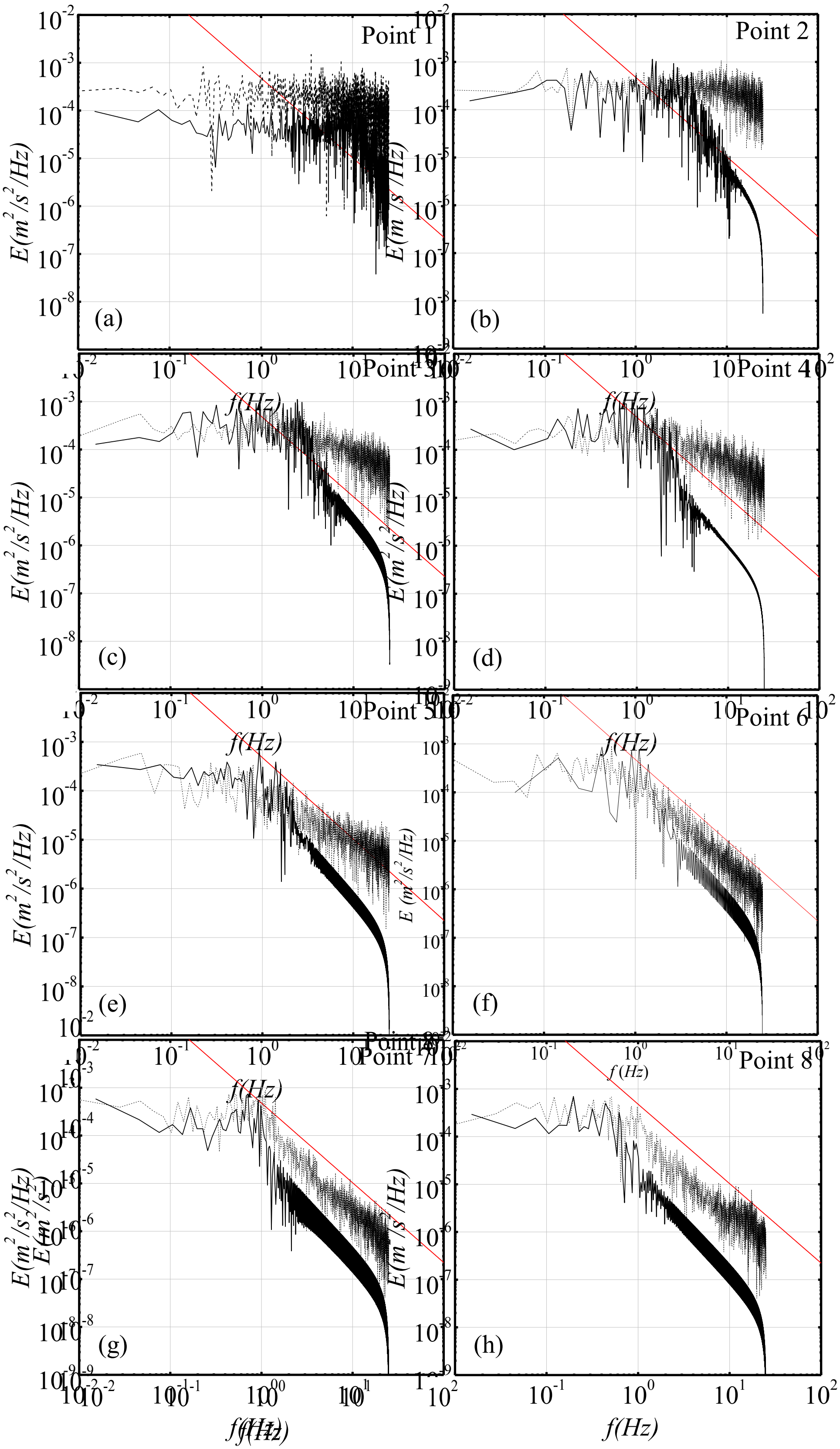
Point 1
Point 2
Point 3
Point 4
Point 5
Point 6
Point 7
Point 8
(a)
(b)
(c)
(d)
(e)
(f)
(g)
(h)
$E(m^2/s^2/Hz)$
$f(Hz)$
10^{-2}
10^{-3}
10^{-4}
10^{-5}
10^{-6}
10^{-7}
10^{-8}
10^{-9}
10^{-1}
10^{0}
10^{1}
10^{2}

Figure 26

List of Tables

Table 1 Experimental conditions

Test No.	D [mm]	U_0 [m/s]	ρ_0 [kg/m^3]	ρ_a [kg/m^3]	g_0' [m/s^2]	Re	Fr
F1	8.0	0.53	1028	998.5	0.30	4240	11.0
F2	8.0	0.58	1028	998.5	0.30	4797	12.0
F3	8.0	0.98	1028	998.5	0.30	7840	20.4
F4	8.0	1.06	1028	998.5	0.30	8480	22.0
F5	8.0	1.45	1028	998.5	0.30	11600	30.1
F6	5.8	0.67	1033	998.5	0.34	3886	15.1
F7	5.8	0.75	1033	998.5	0.34	4350	16.9
F8	5.8	0.84	1033	998.5	0.34	4872	18.9
F9	5.8	0.86	1030	997.3	0.32	5046	20.0
F10	5.8	0.89	1032	997.1	0.34	5162	20.0
F11	5.8	1.08	1030	997.3	0.32	6235	25.0
F12	5.8	1.29	1030	997.6	0.32	7482	30.0
F13	5.8	1.51	1030	997.6	0.32	8737	35.0

Table 2 Numerical conditions

Case No.	D [mm]	U_0 [m/s]	ρ_0 [kg/m^3]	ρ_a [kg/m^3]	g_0' [m/s^2]	Re	Fr	Number of computing CPU core	Number of grids points (million)	Run time (days) for 120s
N1A	8.0	0.53	1028	998.5	0.30	4240	11.0	96	8	8
N1B	8.0	0.53	1028	998.5	0.30	4240	11.0	96	10	12
N6A	5.8	0.66	1030	997.6	0.32	3842	15.1	96	16	18
N9A	5.8	0.86	1030	997.3	0.32	5046	20.0	16	8	12
N9B	5.8	0.86	1030	997.3	0.32	5046	20.0	96	10	12
N9C	5.8	0.86	1030	997.3	0.32	5046	20.0	96	16	17
N11A	5.8	1.08	1030	997.3	0.32	6235	25.0	16	10	10
N11B	5.8	1.08	1030	997.3	0.32	6235	25.0	96	16	17
N12A	5.8	1.51	1030	997.6	0.32	8737	30.0	96	10	12
N12B	5.8	1.51	1030	997.6	0.32	8737	30.0	96	16	18